ADDRESSING CURRENT LIMITATIONS IN DUAL-ENERGY COMPUTED TOMOGRAPHY

A Dissertation
Presented to
The Academic Faculty

By

Michael J. Petrongolo Jr

In Partial Fulfillment
of the Requirements for the Degree
Doctor of Philosophy in the
School of Mechanical Engineering

Georgia Institute of Technology

August 2017

ADDRESSING CURRENT LIMITATIONS IN DUAL-ENERGY COMPUTED TOMOGRAPHY

Approved by:

Dr. Lei Zhu, Advisor
School of Mechanical Engineering
Georgia Institute of Technology

Dr. C.-K. Chris Wang
School of Mechanical Engineering
Georgia Institute of Technology

Dr. Eric Elder
Department of Radiation Oncology
Emory University

Dr. Justin Roper
Department of Radiation Oncology
Emory University

Dr. Xiangyang Tang
Department of Radiology and Imaging Sciences
Emory University

Date Approved: April 11, 2017

I dedicate this work to the love and support shown to me by my family in all facets of life including my academic career and in a special way to my daughter, Angelina.

ACKNOWLEDGEMENTS

TABLE OF CONTENTS

LIST OF TABLES

LIST OF FIGURES

LIST OF SYMBOLS AND ABBREVIATIONS

α, β	regularization weights for PM-DECT
δ	parameter controlling Gaussian kernel widths for IDEM method
ϵ	parameter controlling pixel neighborhood size for IDEM method
η	ratio of low energy to high energy projection data for PM-DECT
λ	singular value of covariance matrix for basis materials
μ	linear attenuation coefficient
$\overrightarrow{\nu}$	indicator of pixels with few similar surrounding pixels in PM-DECT
ξ	parameter controlling strength of spatial filtration in PM-DECT
ρ_e	electron density
Σ	diagonal matrix in singular value decomposition
σ	standard deviation of image pixel values
ψ	rotation angle of X that minimizes entropy
Ω_i	set of pixels similar to pixel i in PM-DECT
A	basis material decomposition matrix
a, b, c, d	elements of A^{-1}
D	geometric distance between two pixels
$E(\%)$	average percent error
F	measured FWHM in a histogram for IDEM method

G	dimension of search region for similar pixels in PM-DECT
h	parameter controlling Gaussian kernel widths for PM-DECT
I	identity matrix
M	forward projection matrix
$\overrightarrow{p}$	histogram from which entropy is calculated
Q	covariance matrix for high and low energy CT images
R	regularization function
$\overrightarrow{s}$	measured sinogram
U, V	rotation matrices in singular value decomposition
W	weighting matrix used for regularization in PM-DECT
w	total number of image pixels
X	matrix containing all pixel values of both decomposed images
x	unitless density of a basis material
Y	X rotated by ψ to minimize entropy in one direction
$\overrightarrow{y}$	a row from the matrix Y
COM	center-of-mass
CBCT	cone beam computed tomography
CT	computed tomography
DECT	dual-energy computed tomography
FBP	filtered backprojection
FWHM	full width at half maximum
HU	Hounsfield units

IDEM	image-domain decomposition through entropy minimization
LDPE	low density polyethylene
NPS	noise power spectrum
PM-DECT	primary modulation based DECT
PMP	polymethylpentene
RMS	root mean square
ROI	region of interest
SNR	signal-to-noise ratio
STD	standard deviation
SVD	singular value decomposition

SUMMARY

Dual-energy computed tomography (DECT) provides better material differentiation compared to conventional CT. However, DECT is fundamentally limited by noise amplification and the burden of dual dataset acquisition. Noise amplification during signal decomposition significantly limits the utility of basis material images while the need for projection data with two different effective x-ray spectra restricts DECT applications to specialized scanners.

Conventional noise suppression algorithms limit signal variation between neighboring pixels which inevitably sacrifices spatial resolution. For noise suppression in DECT, we propose an <u>I</u>mage-domain <u>D</u>ecomposition method through <u>E</u>ntropy <u>M</u>inimization (IDEM). By minimizing entropy in a 2D scatter plot of decomposed pixel values, the IDEM method exploits strong signal correlations and reduces image noise without constraining signal variation between neighboring pixels. As supported by phantom and patient studies, this feature endows our algorithm with a unique capability of reducing noise standard deviations on DECT decomposed images by approximately one order of magnitude while preserving spatial resolution and image noise power spectra.

To address the limitation imposed by data acquisition, we propose a hardware-based acquisition method known as PM-DECT, which utilizes primary beam modulation to enable single-scan DECT on conventional CT scanners. PM-DECT uses an attenuation sheet with a spatially varying pattern, known as a primary beam modulator, to selectively harden an x-ray beam, thereby increasing the average photon energy at specific detector pixel locations. High and low energy images are generated from the sparse datasets via a unique iterative reconstruction algorithm. Phantom studies demonstrate that PM-DECT retains a high level of spatial resolution compared to conventional CT scans and can achieve electron density values with approximately 1% error. Granting the opportunity for high-quality single-scan DECT on conventional CT scanners via limited hardware modification, PM-DECT has the

potential to liberate DECT from specialized scanners, extending clinical availability.

CHAPTER 1

INTRODUCTION

Dual-energy computed tomography (DECT) has improved capability of differentiating between different materials compared to conventional CT [1]. For decades, the clinical implementations of DECT have been hindered mainly by inconsistent CT density values and long scan time [1]. Recent advances in CT technologies, especially the launch of dual-source CT, significantly improve the CT image quality and scan speed. DECT has been increasingly used for automatic bone removal [2, 3], iodine quantification [4, 5], material characterization [6, 7, 8], creating monochromatic images [9, 10], and virtual non-enhanced imaging [11, 12, 13]. The clinical applications have a continuously growing list, including diagnosis of aortic pathologies [14], lung perfusion and ventilation imaging [15], neurological and cerebral vascular imaging [16, 17], and kidney stone characterization [6, 7, 8].

The x-ray photon attenuation of a material resulting from one type of interaction mechanism can be described by a universal energy-dependent function. Therefore, the total photon attenuation of an object is a weighted summation of several known energy-dependent functions for different types of interactions, with weights determined by the material composition of the object [18]. In the diagnostic energy range, x-ray photon interactions with matter are dominated by photoelectric absorption and Compton scattering. Thus, we can decompose the contributions from the two interaction modes using two CT scans with different x-ray spectra - a technique commonly known as DECT. As compared to conventional CT, DECT provides a more complete characterization of an object's attenuation properties and aids material differentiation.

Despite recent clinical success, DECT is fundamentally limited by noise amplification during signal decomposition and the need for an additional dataset as compared to con-

ventional single-source CT. Noise amplification during signal decomposition significantly limits the utility of basis material images. To reduce noise, conventional algorithms limit signal variation between neighboring pixels which inevitably sacrifices spatial resolution. The first part of this dissertation presents an algorithm designed for DECT with unique features of effective noise suppression without degradation of spatial resolution and minimal effect on noise power spectra (NPS). Signal variations are reduced by globally minimizing the entropy of DECT images rather than minimizing the difference between neighboring pixels. The method's strengths are demonstrated on phantom and patient studies.

The need to acquire projection data with two different x-ray spectra restricts DECT applications to specialized scanners. Using a standard CT scanner to perform two scans can lead to artifacts that degrade decomposed images. DECT scanners, which employ specialized hardware components, are costly and are not ubiquitously available in hospitals, reducing the clinical implementations of DECT. The second part of this dissertation investigates a practical hardware-based approach to enable DECT on conventional single-source CT scanners by simultaneously acquiring high and low energy projection data during a single scan. This is accomplished using an attenuation sheet, known as a primary modulator, inserted into the x-ray path to modify the beam spectrum. Phantom studies demonstrate that a single CT scan with primary beam modulation can generate high quality CT images while yielding DECT results that largely retain spatial resolution and limit error.

1.1 Main Contributions and Publications

The work contained within this dissertation and other research performed as part of my studies at the Georgia Institute of Technology have produced the following first authorships on journal papers:

- **M. Petrongolo** and L. Zhu, "'Noise suppression for dual-energy CT through entropy minimization," *IEEE Transactions on Medical Imaging*, vol. 34, no. 11, pp. 2286-2297, 2015.

- **M. Petrongolo**, X. Dong, and L. Zhu, "A general framework of noise suppression in material decomposition for dual-energy CT," *Medical Physics*, vol. 42, no. 8, pp. 4848-4862, 2015.

as well as contributions on a number of other publications:

- X. Dong, **M. Petrongolo**, T. Niu, and L. Zhu, "Low-dose and scatter-free cone-beam CT imaging using stationary beam blocker in a single scan: phantom studies," *Computational and Mathematical Methods in Medicine*, vol. 2013, Article ID 637614, 8 pages, 2013.

- T. Niu, X. Dong, **M. Petrongolo**, and L. Zhu, "Iterative image-domain decomposition for dual-energy CT," *Medical Physics*, vol. 41, no. 4, 041901, 2014.

- T. Niu, X. Ye, Q. Fruhauf, **M. Petrongolo**, and L. Zhu, "Accelerated barrier optimization compressed sensing (ABOCS) for CT reconstruction with improved convergence," *Physics in Medicine and Biology*, vol. 59, no. 7, pp. 1801-1814, 2014.

- J. Harms, T. Wang, **M. Petrongolo**, and L. Zhu, "Noise Suppression for dual-energy CT via penalized weighted least-square optimization with similarity-based regularization," *Medical Physics*, vol. 43, no. 5, pp. 2676-2686, 2016.

and conference presentations:

- **M. Petrongolo**, T. Niu, and L. Zhu, "Noise suppression for dual-energy CT through entropy minimization," John R. Cameron Young Investigator Symposium, *AAPM Annual Meeting*, July 2014.

- **M. Petrongolo** and L. Zhu, "Improved Noise suppression for dual-energy CT through entropy minimization," *AAPM Annual Meeting*, July 2015.

- **M. Petrongolo** and L. Zhu, "Single-scan dual-energy CT using primary modulation," *AAPM Annual Meeting*, July 2015.

When this dissertation was written, a manuscript covering the work presented in Chapter 3 was under consideration by *IEEE Transactions on Medical Imaging* for publication.

CHAPTER 2

NOISE SUPPRESSION FOR DUAL-ENERGY CT THROUGH ENTROPY MINIMIZATION

2.1 Introduction

In the practical implementation of DECT, signal decomposition is commonly performed using two known basis materials in either the projection domain [18, 19, 20, 21] or image domain [9, 22, 23]. Projection-domain decomposition has the advantage of effective beam hardening correction if a non-linear decomposition is used, but it requires access to raw projection data [18, 21]. Image domain decomposition directly operates upon CT images [9, 22, 23], and its implementation is more convenient on clinical CT scanners [9, 22]. DECT on a dual-source CT scanner is one particular example where image-domain decomposition is considered advantageous. Due to the orthogonal direction of the two x-ray beams of different energies, it is difficult to accurately obtain two measurements for the same projection ray for projection-domain decomposition [1, 9, 24]. In this chapter, we focus on DECT with image-domain decomposition.

The decomposition procedure of DECT is highly sensitive to noise mainly because x-ray spectra at different tube voltages and energy distributions of linear attenuation coefficients of basis materials both have significant overlap in the diagnostic x-ray energy range. It has been shown that if a primitive decomposition method is employed, the signal-to-noise ratios (SNR) on decomposed images of basis materials are significantly lower than those on the original CT images [25, 26]. Noise amplification, a well-known issue since the invention of DECT [27, 28], has become the last hurdle toward quantitative use of DECT in clinical applications.

Existing low-dose CT techniques, including both hardware and software improvements,

reduce noise of DECT. More sophisticated algorithms consider redundant structural information and signal statistics of dual-energy scans and embed noise suppression into the signal processing chain of DECT. For example, Warp *et al.* used the low-energy CT image to determine edge locations and then adaptively smoothed the high energy CT image while preserving bone edges at the predetermined locations [29]. Kalendar *et al.* proposed to minimize the noise of decomposed images based on its negative correlation [27]. Balda *et al.* developed a joint intensity statistical method on CT images prior to decomposition [30]. Recently, we have improved an iterative CT reconstruction algorithm [31] for enhanced noise suppression performance in DECT, by combining iterative CT reconstruction with the decomposition of DECT [25]. We have developed another iterative algorithm for DECT noise suppression, which is applied directly on CT images to avoid the computationally intensive reconstruction [26]. The algorithm fully explores the noise statistical properties of the decomposition process by combining noise suppression and material decomposition into an iterative process.

A common feature of most existing algorithms, including those previously developed in our group, is that they aim to reduce noise of one pixel by limiting signal variation compared with adjacent pixels. Prior knowledge or estimation of noise statistics and edge constraints help to selectively suppress the noise in a small neighborhood to avoid errors on true signals. However, in using spatial distributions, these methods inevitably sacrifice spatial resolution and alter image NPS by preferentially suppressing high-frequency noise, as shown in the results section of this chapter. Shifting the NPS towards low-frequency noise leads to different image texture with the appearance of coarser noise [32] and potentially degrades object detectability [33, 34]. We aim to break the tradeoff between noise suppression and spatial resolution in the signal processing of DECT and to substantially reduce DECT noise without altering image NPS. Toward this goal, we abandon the design principle of denoising algorithms that attempt to reduce signal variations between neighboring pixels. Instead, we aim to limit signal variation within the same material. We improve

material differentiation of DECT on noisy decomposed images via a new technique of entropy minimization. The image noise is effectively reduced by exploiting noise correlation properties. The performance of the proposed method, henceforth referred to as IDEM (Image-domain Decomposition through Entropy Minimization), is assessed using phantom and patient studies. Electron density calculations are used to quantify its accuracy. The results are compared to those without noise suppression, with a filtering method [35], and with an iterative method developed in our group [26].

2.2 Method

2.2.1 Noise Propagation in DECT Decomposition

In this section, we first analyze noise amplification in DECT decomposition. The property of strong noise correlation on decomposed images is then investigated.

We study DECT in the diagnostic energy range with image-domain decomposition. Each DECT dataset contains two CT images at different energy levels, henceforth referred to as high and low energy images. We assume that the two CT images are acquired independently and therefore have independent noise. Thus, each pixel location has a pair of corresponding values, one from the high energy image (μ_h) and the other from the low energy image (μ_l). We consider a pair of attenuation coefficients (μ_h, μ_l) to be a linear combination of two known basis materials, yielding the following relationship:

$$\overrightarrow{\mu} = A \overrightarrow{x} \tag{2.1}$$

where $\overrightarrow{\mu} = [\mu_h \ \mu_l]^T$, $\overrightarrow{x} = [x_1 \ x_2]^T$, and

$$A = \begin{bmatrix} \mu_{1h} & \mu_{2h} \\ \mu_{1l} & \mu_{2l} \end{bmatrix}. \tag{2.2}$$

μ_{1h}, μ_{2h}, μ_{1l}, and μ_{2l} represent the high and low energy attenuation coefficients for basis

materials 1 and 2, and x_1 and x_2 are the unitless densities of basis materials 1 and 2, respectively. Directly solving Eqn. (2.1) gives the pixel values of the decomposed images as:

$$\vec{x} = A^{-1}\vec{\mu}. \tag{2.3}$$

Signal SNR significantly drops on the decomposed images obtained by Eqn. (2.3). To see this, we note that:

$$A^{-1} = \frac{1}{\det(A)} \begin{bmatrix} \mu_{2l} & -\mu_{2h} \\ -\mu_{1l} & \mu_{1h} \end{bmatrix}. \tag{2.4}$$

The factor $\frac{1}{\det(A)}$ can be ignored in the SNR calculation. Eqns. (2.3) and (2.4) show that the noise variance of the decomposed images is the summation of noise variances of CT images weighted by the square of linear attenuation coefficients of the basis materials. On the other hand, the signals in decomposed images become $\mu_h\mu_{2l} - \mu_l\mu_{2h}$ or $-\mu_h\mu_{1l} + \mu_l\mu_{1h}$. Therefore, with clinically relevant values of linear attenuation coefficients, decomposition using Eqn. (2.3) often results in large signal cancellations. A scenario for relatively small signal cancellation is when decomposing a pixel onto the basis image of its own material. However, even these best-case scenarios lead to large SNR degradation after image decomposition.

Besides noise boost, one property of decomposed images is that their noise is highly correlated [27]. For analysis simplicity, we assume that the noise of one pixel on the high and low energy CT images is Gaussian, i.e. $\vec{\mu} \sim \mathcal{N}(\vec{\mu_0}, Q)$, where $\vec{\mu_0}$ is the mean value and the covariance matrix, Q, is defined as follows:

$$Q = \begin{bmatrix} \sigma_h{}^2 & 0 \\ 0 & \sigma_l{}^2 \end{bmatrix}. \tag{2.5}$$

σ_h and σ_l are the standard deviations (STDs) of independent noise associated with the high and low energy images, respectively. Based on Eqn. (2.3), we obtain the probability density

distribution of the decomposed images: $\vec{x} \sim \mathcal{N}\left(A^{-1}\vec{\mu_0}, A^{-1}Q\left(A^{-1}\right)^T\right)$ [26]. This shows that the decomposed images are jointly Gaussian, with an elliptical and highly asymmetric (i.e., highly correlated) distribution as specified by the covariance matrix $A^{-1}Q\left(A^{-1}\right)^T$.

To see this, we first note that:

$$A^{-1}Q\left(A^{-1}\right)^T = A^{-1}Q^{\frac{1}{2}}\left(A^{-1}Q^{\frac{1}{2}}\right)^T = A'(A')^T \tag{2.6}$$

where,

$$A' = A^{-1}Q^{\frac{1}{2}}. \tag{2.7}$$

Singular value decomposition (SVD) gives:

$$A' = U\Sigma V^T \tag{2.8}$$

where U and V are unitary matrices, and Σ is a diagonal matrix whose entries are singular values of A'. Therefore, we can rewrite the covariance matrix as:

$$A^{-1}Q\left(A^{-1}\right)^T = U\Sigma V^T V\Sigma^T U^T = U\Sigma\Sigma^T U^T. \tag{2.9}$$

As such, the condition number of the covariance matrix, or the eccentricity of the joint Gaussian distribution, is totally determined by Σ.

Exerting SVD on A', we obtain the singular values of $A^{-1}Q\left(A^{-1}\right)^T$ as:

$$\lambda_{1,2} = \frac{z \pm \sqrt{z^2 - 4\left(\sigma_h\sigma_l\mu_{1h}\mu_{2l} - \sigma_h\sigma_l\mu_{2h}\mu_{1l}\right)^2}}{2} \tag{2.10}$$

where

$$z = \left(\sigma_h\mu_{2l}\right)^2 + \left(\sigma_l\mu_{2h}\right)^2 + \left(\sigma_h\mu_{1l}\right)^2 + \left(\sigma_l\mu_{1h}\right)^2. \tag{2.11}$$

Using Taylor's expansion, we simplify Eqn. (2.10) via the following approximation:

$$\sqrt{g^2 - \Delta} \approx g - \frac{\Delta}{2g} \qquad (2.12)$$

where g is positive and Δ is a small value compared to g. The condition number of $A^{-1}Q\left(A^{-1}\right)^T$ is finally approximated as:

$$\frac{\lambda_1}{\lambda_2} \approx \left(\frac{z}{\sigma_h \sigma_l \mu_{1h} \mu_{2l} - \sigma_h \sigma_l \mu_{2h} \mu_{1l}}\right)^2 - 1 \; . \qquad (2.13)$$

For practical values in DECT, the denominator of the first term of Eqn. (2.13) is close to zero, which drives $\frac{\lambda_1}{\lambda_2}$ to be much greater than 1. For example, since σ_l and σ_h are typically on the same order of magnitude, the above approximation gives $\frac{\lambda_1}{\lambda_2}$ values on the order of 10^3 if we assign the values for epoxy and aluminum (i.e., two basis materials used in the presented studies of this paper) at tube potentials of 75 kVp and 125 kVp, i.e., $\{0.024, 0.084, 0.022, 0.065\}$ mm^{-1}, to the linear attenuation coefficients used in the material decomposition, $\{\mu_{1l}, \mu_{2l}, \mu_{1h}, \mu_{2h}\}$. The estimated condition number is consistent with the measured values in our experiments.

To better demonstrate the effect that a large condition number has on decomposed image noise, Fig. 2.1 shows low and high energy CT images as well as 2D scatter plots of pixel values before and after DECT decomposition. Each pixel pair in Fig. 2.1a corresponds to one data point in the plots of Figs. 2.1b and 2.1c. Due to independent noise in CT images, the image pixels of one material form an elliptical cluster in a 2D scatter plot of pixel values as seen in Fig. 2.1b. Note, the pixel values of CT images are in Hounsfield Units (HU), which is converted from the linear attenuation coefficient μ as:

$$HU = \frac{\mu - \mu_{water}}{\mu_{water}} \times 1000 \qquad (2.14)$$

where μ_{water} is the linear attenuation coefficient of water in the CT image. As illustrated

in Fig. 2.1c, DECT decomposition forces the material clusters into a highly asymmetric shape, dramatically prolonging them in the direction of signal correlation. In this paper, we aim to suppress noise on decomposed material images by utilizing the eccentric statistical distribution.
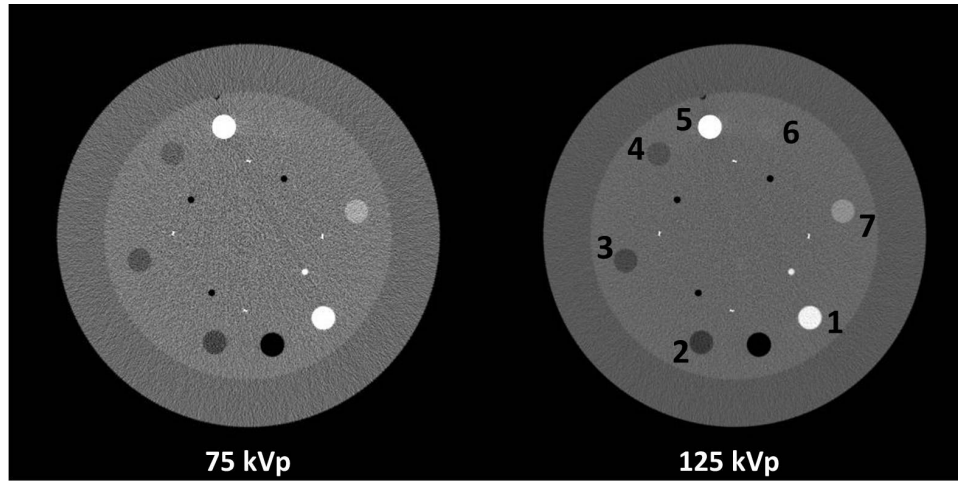
(a)
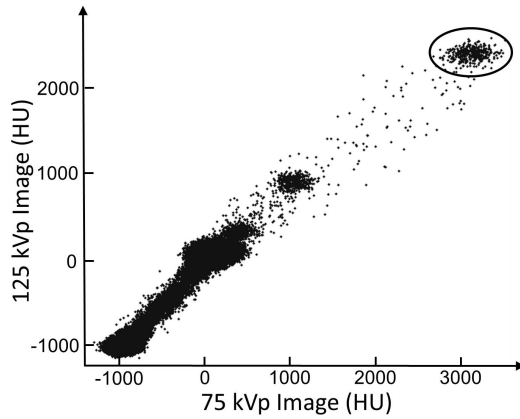
(b)
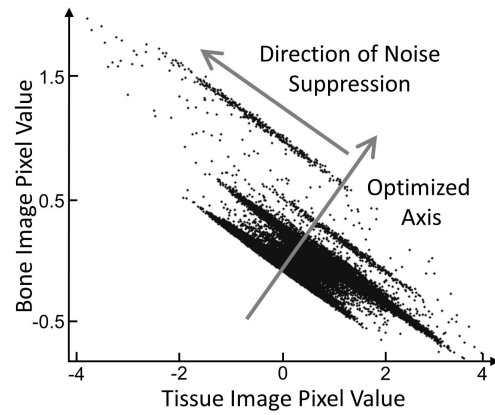
(c)

Figure 2.1: (a) CT images of the contrast-rod slice of the Catphan©600 phantom accompanied by 2D scatter plots of pixels (b) before and (c) after DECT decomposition. The numbered materials are: [1] Teflon, [2] polymethylpentene (PMP), [3] low density polyethylene (LDPE), [4] Polystyrene, [5] aluminum, [6] acrylic, and [7] Delrin. The circled area in (b) indicates a group of data points from the aluminum rod. The arrows in (c) show the optimized axis and the direction of noise suppression in the IDEM algorithm. Display window for (a) is [-500 1000] HU.

2.2.2   Noise Suppression through Entropy Minimization

Noise suppression is possible when redundant information is explored on the measurements. Existing algorithms reduce noise in data of a single measurement by implicitly assuming similar noise statistics for neighboring pixels. Novel methods have been developed to exclude pixels (e.g., edges) with highly different statistics from noise suppression. However, as long as a method relies on the spatial relationship of signals, it is difficult, if not impossible, to eliminate all associated errors, including spatial resolution loss and degraded NPS [36].

Since the accuracy of CT imaging has been significantly improved by recent advances on CT hardware, reconstruction algorithms, and correction algorithms, pixels representing the same material have consistent values and noise statistics on CT images and thus on DECT decomposed images. We propose using the material, or entropy property, of the imaged object for noise reduction on DECT, i.e., the IDEM method. Pixels representing similar materials are first estimated and grouped. Noise suppression is then carried out on these pixels by utilizing the noise correlation between the decomposed images.

Here we describe the design principle and workflow of the IDEM algorithm. More implementation details will be included in the next section. If decomposed images were to contain negligible noise, the 2D scatter plot of these decomposed images should reveal tight clusters about different centers-of-mass (COM) for different materials. Based on this concept, to reduce noise boost during decomposition, we propose an entropy-minimization based algorithm, outlined in Fig. 2.2. We first search for an axis passing through the origin in the 2D scatter plot of decomposed images, on which the projection of all data points has minimal entropy. This optimized axis specifies the direction that the magnified noise minimally increases the image entropy. Next, we implement an empirical noise suppression procedure in the direction perpendicular to the axis of minimum entropy as indicated in Steps 2 and 3 of Fig. 2.2. For each pair of pixels on decomposed images at the same location, $\vec{x}$, we project the data point in the scatter plot onto the optimized axis. Pixels

of similar materials are identified if their projections onto the optimized axis are within a small neighborhood around the projection of $\overrightarrow{x}$. We then calculate the COM value, $\overrightarrow{x_c}$, for this pixel group. $\overrightarrow{x}$ is finally replaced by $\overrightarrow{x_c}$ for noise suppression. The optimal axis in the 2D scatter plot and the direction of noise suppression are indicated in Fig. 2.1c.

Signal bias appears on the noise-suppressed images if pixels of different materials are grouped together for the COM calculation. Generally, including more pixels in the COM calculation increases the strength of noise suppression but also the possible bias. This tradeoff can be likened to those in other noise suppression techniques, such as filtering or gradient-based iterative methods, where stronger noise suppression typically leads to poorer image spatial resolution. As discussed in detail in the next section, two strategies are proposed to improve the accuracy of material differentiation and thus to reduce image bias. We differently weight the contribution of each pixel to the COM calculation such that pixels with CT values close to (or far from) the CT values at the location of $\overrightarrow{x}$ have high (or low) influence. A spatial weighting technique is also designed as an option in the IDEM algorithm to further alleviate error for pixels that have close CT values but are spatially distant.

2.2.3   Implementation Details

In this section, we provide a detailed explanation for each step of the IDEM algorithm shown in Fig. 2.2, with examples of pseudo codes for two-dimensional images.

Fig. 2.3 shows the pseudo code for Step 1 (i.e., finding the optimal axis onto which the projection of data clusters has minimum entropy) with parameter values used in our implementations. The orientation of the optimal axis is primarily determined by the unitary matrix U in Eqn. (2.9), which depends on both the decomposition matrix A and the covariance matrix Q. However, Q is determined by the unknown noise STDs of the high and low energy CT images. To provide an initial estimate of the angle of the optimal axis, we assume that noise STDs in the high and low energy images are approximately equal,
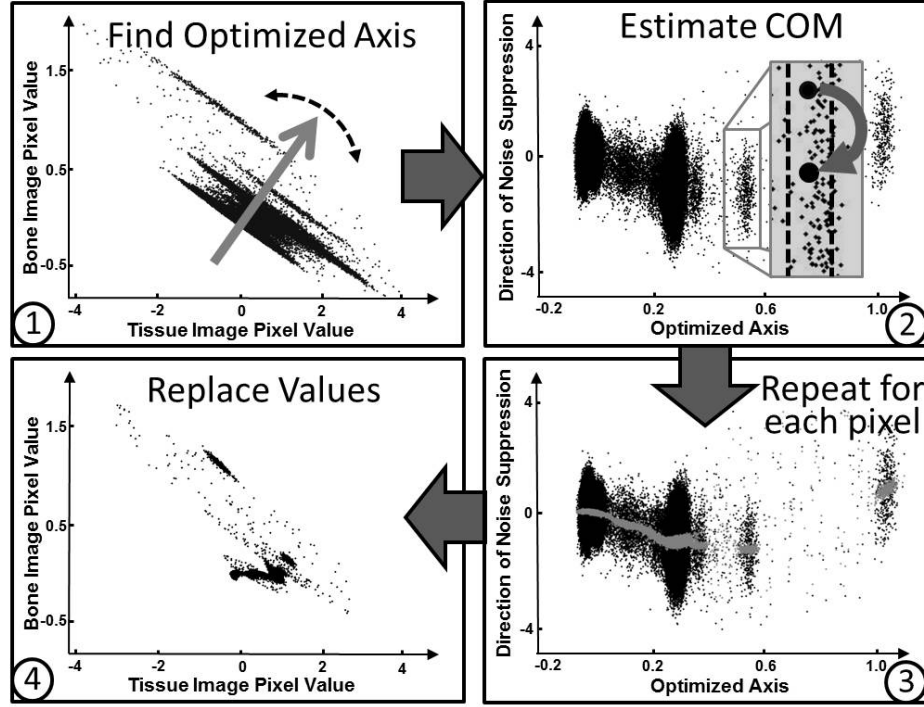
Figure 2.2: Outline of the IDEM method. The plot in Step 2 depicts the same data points as those in Step 1 rotated about the origin so that the optimized axis is horizontal. Note that different scales are used on the axes of the subfigures for improved clarity. In Step 3, the grey points are the COM estimates that will replace the black points.

which changes Eqn. (2.7) to:

$$A' \approx \sigma A^{-1} \tag{2.15}$$

where σ is a scalar and does not affect the unitary matrices determined through SVD. Thus, we can estimate the optimal angle via SVD on A^{-1}. We refine this value using a brute-force algorithm to search amongst neighboring angles for the value achieving minimum entropy (lines 8-14 in Fig. 2.3). The entropy of a histogram, $\overrightarrow{p}$, with n bins is calculated as shown in line 12. The angle onto which the projection of all data points has the minimum entropy is selected as the optimal, and all data points in the scatter plot are rotated by that angle, ψ.

Step 1 outputs a 2-by-w matrix Y, where w is the total number of image pixels. The majority of noise amplification from decomposition is now confined to the second row of Y, $\vec{y}_2$, while the first row of Y, $\vec{y}_1$, can be used as an indicator of different materials. We

	%User-defined parameters.
1	$\gamma = 5°$; %Range of search
2	$\kappa = 0.01°$; %Step size between angles
3	$n = 256$; %Number of histogram bins
4	$w = 512^2$; %Number of image pixels
	%Initialize variables.
5	$X = [\vec{x_1}\ \vec{x_2}]^T$, $H = 0$;
	%Perform SVD on A^{-1} and obtain an angle estimate.
6	$U\Sigma V^T = A^{-1}$;
7	$\phi = \cos^{-1}(U(1,1)) - 90°$;
	%Search angles in the neighborhood of ϕ.
8	**for** $\theta = \phi - \gamma : \kappa : \phi + \gamma$
9	$T = \begin{bmatrix} \cos(\theta) & -\sin(\theta) \\ \sin(\theta) & \cos(\theta) \end{bmatrix}^T X$;
10	$\vec{p} = \text{1DHist}([T(1,1)\ T(1,2)\ \ldots\ T(1,w)], n)$;
	%Find orientation with the smallest entropy, H.
11	**if** $\left(\theta == \phi - \gamma \text{ or } \sum_{i=1, \vec{p}(i) \neq 0}^{n} -\log(\vec{p}(i)) < H \right)$
12	$\psi = \theta$, $H = \sum_{i=1, \vec{p}(i) \neq 0}^{n} -\log(\vec{p}(i))$;
13	**end**
14	**end**
	%Rotate X by optimal angle, ψ.
15	$Y = \begin{bmatrix} \cos(\psi) & -\sin(\psi) \\ \sin(\psi) & \cos(\psi) \end{bmatrix}^T X$;
	%Output ψ, and the rotated pixel values Y
16	**output** ψ, Y

Figure 2.3: Pseudo code for Step 1 of Fig. 2.2. In line 10, 1DHist($\vec{T}, n$) is a function that converts a vector $\vec{T}$ into a histogram normalized by the total number of points, with n histogram bins.

therefore use $\vec{y}_1$ for material classification and perform noise suppression on $\vec{y}_2$.

Fig. 2.4 shows the pseudo code for Steps 2-4 of the IDEM algorithm. To improve computation efficiency, we first sort $\vec{y}_1$ in ascending order (line 9). For each image pixel, a group of pixels is selected such that their $\vec{y}_1$ values are in a small neighborhood (lines 12-18). The neighborhood size is set to be $\epsilon \cdot F$, where ϵ is a user-defined parameter ($0.5 \sim 1.5$ in our implementations) and F is the measured full-width-at-half-maximum (FWHM) of one major peak in the histogram of $\vec{y}_1$. Note that since $\vec{y}_1$ values are pre-sorted, the search range for neighboring pixels is small and is adaptively changed for each search. We suppress image noise by calculating the COM in the direction perpendicular to the optimal axis using the $\vec{y}_2$ values of all pixels identified as one group. To improve algorithm accuracy in the presence of material classification errors, we weight each value of $\vec{y}_2$ differently in the COM calculation (line 25). The weight assigned to one pixel (with index "a") inside the neighborhood of a different pixel (with index "b") is calculated using two schemes shown in lines 19-24. The first weight is calculated in line 19, using a Gaussian function of CT value differences for pixels "a" and "b" on the high and low-energy CT images. The width of Gaussian kernel is controlled by $\delta \cdot \hat{\sigma}$, where δ is a user-defined parameter and $\hat{\sigma}$ is the estimated or measured noise STD in a CT image. Line 22 calculates a second and optional weight, which uses an empirical function of geometric distance, D, between pixels "a" and "b". Pixels with close CT values and geometric distance (if the spatial weighting is enabled) are considered more likely to be of the same material and therefore contribute more to the COM calculation. The calculated COM value then replaces the value of $\vec{y}_2$ at pixel index "b" (line 27). Noise suppressed images of decomposed materials are finally obtained after undoing the operations of sorting and rotation (lines 27-29).

2.2.4   Selection of Algorithm Parameters

All the control parameters of the IDEM algorithm and their values in our implementations are shown in the pseudo codes of Figs. 2.3 and 2.4. In this work, most parameter values

1	ψ, Y; %From the outputs of Step 1.
2	$\epsilon = 0.5 \sim 1.5$; %Control the neighborhood size.
3	$\delta = 3 \sim 30$; %Control the Gaussian kernel widths.
4	$w = 512^2$; %Number of image pixels.
5	$\tau = 15, \zeta = 2.5e - 3$; %Spatial weighting parameters.
6	$spatial = 1, 0$; %Is spatial weighting enabled?
7	$\hat{\sigma}_h, \hat{\sigma}_l$; %Estimated noise STDs on high and low-energy CT.
8	F; %FWHM of one peak in the histogram of $Y(1, :)$.
9	$N = sort(Y(1, :)), k = 1$; %Sort $Y(1, :)$ in ascending order; Output sorted index N.
10	**for** $v = 1 : w$
11	$\quad m = 0, flag = 0, \overrightarrow{C} = [\ ]$;
12	$\quad$ **for** $i = k : w$, %Find pixels in the neighborhood.
13	$\quad\quad$ **if** $|Y(1, N(v)) - Y(1, N(i))| < \epsilon \cdot F$
14	$\quad\quad\quad$ **if** $(!flag), k = i, flag = 1$, **end;**
15	$\quad\quad\quad m = m + 1, J(m) = I(i)$; %Store pixel index J.
16	$\quad\quad$ **elseif** $flag$, **break;**
17	$\quad\quad$ **end**
18	$\quad$ **end**
	$\quad$ %Produce weights based on CT images.
19	$\quad$ **for** $i = 1 : m, \overrightarrow{C}(i) = \textbf{exp}\left(-\frac{\left(\overrightarrow{\mu_h}(J(i)) - \overrightarrow{\mu_h}(N(v))\right)^2}{(\delta\hat{\sigma}_h)^2} - \frac{\left(\overrightarrow{\mu_l}(J(i)) - \overrightarrow{\mu_l}(N(v))\right)^2}{(\delta\hat{\sigma}_l)^2} \right)$; **end;**
20	$\quad$ **if** $spatial$
21	$\quad\quad$ **for** $i = 1 : m$
22	$\quad\quad\quad D = distance(J(i), N(v)); \overrightarrow{C}(i) = \overrightarrow{C}(i) \cdot \left(\frac{\zeta + \exp(-D^2/\tau^2)}{1 + \zeta} \right)$;
23	$\quad\quad$ **end**
24	$\quad$ **end**
25	$\quad \overrightarrow{y_c}(v) = \sum\limits_{i=1}^{m} \overrightarrow{C}(i) \cdot Y(2, J(i)) / \sum\limits_{i=1}^{m} \overrightarrow{C}(i)$; %Calculate COM.
26	**end**
27	$Y(2, N) = \overrightarrow{y_c}$; %Replace $Y(2, :)$ with COM values and undo sorting.
28	$X_f = \begin{bmatrix} \cos(\psi) & -\sin(\psi) \\ \sin(\psi) & \cos(\psi) \end{bmatrix} Y$; %Undo rotation.
29	**output** X_f; %Each row of X_f is a noise-suppressed material image.

Figure 2.4: Pseudo code for Steps 2 through 4 of Fig. 2.2. User-defined and measured parameters are listed in Lines 2-6 and 7-8, respectively. In Line 22, $distance()$ calculates the geometric distance between two pixels with indices of $J(i)$ and $N(v)$.

are fixed and the method performance is controlled by tuning only two parameters: ϵ and δ.

The ϵ value determines the size of the neighborhood used to group pixels for COM calculations. As including more pixels in a COM calculation increases the strength of noise suppression, ϵ is strongly correlated with the level of noise suppression. Stronger noise suppression, however, increases potential errors of image bias. In our studies, we find that ϵ values in the range of $0.5 \sim 1.5$ well balance the strength of noise suppression and the induced image bias errors. The selection of δ balances the same tradeoff by controlling the joint-Gaussian function used to weight a pixel's contribution in the COM calculation based on its CT values. The δ value is inversely correlated with the reliance on CT values for material classification. We find using phantom studies that our method performance is relatively insensitive to the choice of δ values in the range of $3 \sim 10$. We use δ values as high as 30 and 45 in a patient study because the image set contains lower noise levels and thus poses less of a risk for material classification error.

2.2.5   Evaluation

We have assessed method performance using phantom and patient studies. The former were performed using an evaluation phantom, Catphan©600 (The Phantom Laboratory: Salem, NY), and an anthropomorphic head phantom. Projection data were acquired using a tabletop CT system at Georgia Institute of Technology [37], whose geometry matches that of the on-board imager system of a Varian radiation therapy machine. Phantom data were acquired for 655 projection views using tube potentials of 75 kVp and 125 kVp and a tube current of 80 mA. To limit photon scatter, the phantoms were imaged with a narrowly opened collimator, i.e., a fan-beam equivalent geometry. High and low energy CT images were reconstructed using filtered backprojection (FBP), with an image size of 512 by 512 pixels and pixel resolution of 0.5 by 0.5 mm^2. For the patient study, high and low energy CT images were generated from a scan of the head region using a clinical dual-source CT

scanner, i.e., a Siemens SOMATOM Definition Flash. Tube potentials for the DECT scan were 80 kVp and 140 kVp. Our algorithm for noise suppression via entropy minimization typically takes 10 to 20 minutes using MATLAB on a 2.66 GHz CPU workstation.

We compared the IDEM algorithm with a filtering method [35] and an iterative method recently developed in our group by Niu *et al.* [26]. All three methods perform decomposition in the image domain after a standard CT reconstruction using FBP. The filtering method applies a median filter to the high and low energy images prior to material decomposition. This decreases noise in the initial CT images and thus limits the amount of amplified noise in the resultant basis material images. The iterative method formulates the material decomposition of DECT as a least-squares estimation problem, with a regularization term to preserve structural edges and with the inverse of the estimated variance-covariance matrix of the decomposed images as the penalty weight in the least-squares term. We used image noise, NPS, and spatial resolution as image quality metrics in the comparisons. The accuracy of electron density measurements with and without the proposed noise suppression was also investigated.

One slice of the Catphan©600 phantom, which contains high contrast line pairs, was used to evaluate performance on spatial resolution. The line pairs with spatial frequency from 1 to 21 line pairs/cm are made of aluminum, surrounded by epoxy, a water-equivalent material. In the study, basis materials of aluminum and epoxy were chosen to create "bone" and "tissue" images, respectively. A uniform area was selected as the region of interest (ROI) for noise analysis. In addition, the 2D NPS was calculated for an area of uniform material as:

$$NPS \approx |\text{DFT}_2\{f\}|^2 \tag{2.16}$$

where f is the image ROI with pixel values offset to achieve a zero mean value, and $\text{DFT}_2\{f\}$ denotes the 2D discrete Fourier transform of the image [38, 39, 40].

A different slice of the Catphan©600 phantom, which contains rods of different materials, was used to assess the accuracy of electron density measurements. We used epoxy and

aluminum as basis materials to create "tissue" and "bone" images, respectively. Contrast rods were used as ROIs for electron density measurement, calculated as:

$$\rho_e = \rho_{e,b} \cdot x_b + \rho_{e,t} \cdot x_t \tag{2.17}$$

where x_b and x_t are pixel values of decomposed bone and tissue images, and $\rho_{e,b}$ and $\rho_{e,t}$ are the electron densities of the bone and tissue materials, respectively. Note that the decomposed images are unitless and indicate the normalized densities of equivalent basis materials contained inside one pixel. For each rod, the average percent error of associated pixels was determined using the equation:

$$E(\%) = \left(\frac{\overline{\rho_e} - \rho_e^{ref}}{\rho_e^{ref}} \right) \times 100\% \tag{2.18}$$

where ρ_e^{ref} is the true electron density of a rod, which is provided in the Catphan©600 phantom's user manual, and $\overline{\rho_e}$ is the mean value of measured electron density inside the rod. The accuracy of our method as compared to that achieved without noise suppression was assessed using the root mean square (RMS) of the $E(\%)$ of all the rods.

The head phantom was used for comprehensive evaluations of different methods on an object with complicated structures. The head phantom is composed of epoxy mimicking soft tissue and a calcium compound mimicking bone. Note that, the calcium compound has a spatially varying density, producing relatively large entropy in the proposed data processing even if image noise is low. The calcium compound ("bone") and epoxy ("tissue") were chosen as basis materials.

Patient images were used to assess method performance on a clinically relevant dataset. This also provided an opportunity to test performance on images acquired via a scanning system other than CBCT. Soft tissue and bone were chosen as basis materials for this study.

In the presented DECT results, errors in material decomposition stem from sources including beam hardening effects on the CT images and the proposed signal processing.

20

In this work, we focus our research on noise suppression in DECT material decomposition. Beam hardening correction is therefore considered beyond our scope and is not implemented on the resultant images. The results obtained by direct decomposition via Eqn. (2.3) with no noise suppression are used as the ground truth in our investigations on decomposition accuracy of the IDEM algorithm.

2.3 Results

2.3.1 Catphan Study on Spatial Resolution and NPS

Fig. 2.5 shows the 75 kVp and 125 kVp CT images of the line-pair slice of Catphan©600 phantom. The decomposed images using different methods are shown in Fig. 2.6. As indicated by Eqn. (2.3), since the CT images and the elements of the decomposition matrix have the same units, the decomposed images are unitless density maps of the basis materials. Direct decomposition via Eqn. (2.3) results in severe noise amplification, as seen in the first row of Fig. 2.6. SVD on the inverse of the decomposition matrix estimates the angle of the optimal axis for noise suppression to be $73.13°$. The proposed entropy minimization refines this value to $72.24°$. All three methods, including the filtering method [35], the iterative method [26], and the IDEM algorithms, i.e., with and without spatial weighting (SW and NSW, respectively), effectively reduce noise on the decomposed images. Table 2.1 summarizes the mean pixel values and noise STDs of each basis material image within the ROI depicted by the dashed circle in Fig. 2.6. For a fair comparison of performance on spatial resolution, we tune the algorithm parameters such that all the methods achieve similar levels of noise suppression, with reduction of noise STD on both "bone" and "tissue" images by a factor of around 8.5. By inspecting the line-pair images, especially the zoom-in images within Figs. 2.5 and 2.6, we conclude that the proposed entropy minimization based method (both with and without spatial weighting) achieves the best performance on preservation of spatial resolution in both decomposed images. The spatial resolution of the decomposed images via the IDEM method is close to that of the initial CT images.
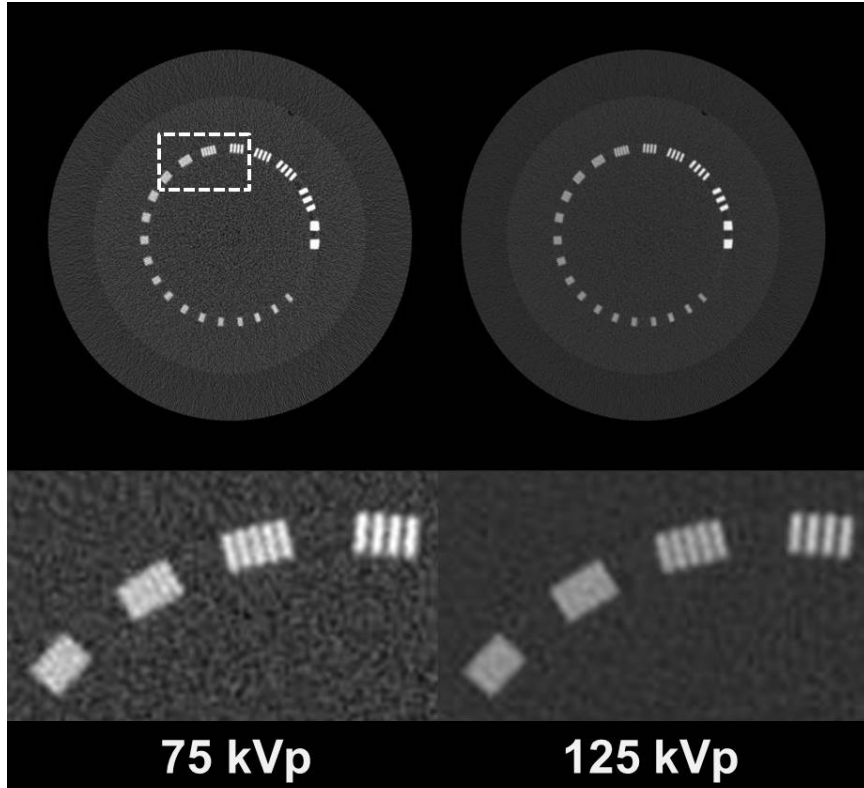
Figure 2.5: Low and high energy CT images of the line-pair slice of Catphan©600 phantom. Zoom-in images of the line pairs are shown in the second row, with spatial frequencies from 5 to 8 line pairs/cm, moving from right to left. The dashed box in the top left image indicates the location where the zoom-in images are taken. Display window: [-500 2500] HU.

Table 2.1: Mean and STD within the ROI (indicated by the dashed circle in Fig. 2.6) of Catphan© line-pair basis material images.

	"Bone" Image	"Tissue" Image
Without Noise Suppression	-0.002 ± 0.3	1.00 ± 0.8
Filtering Method	-0.004 ± 0.04	1.01 ± 0.1
Iterative Method	-0.004 ± 0.04	1.01 ± 0.09
IDEM Method (NSW)	0.003 ± 0.04	0.99 ± 0.09
IDEM Method (SW)	-0.002 ± 0.04	1.00 ± 0.09
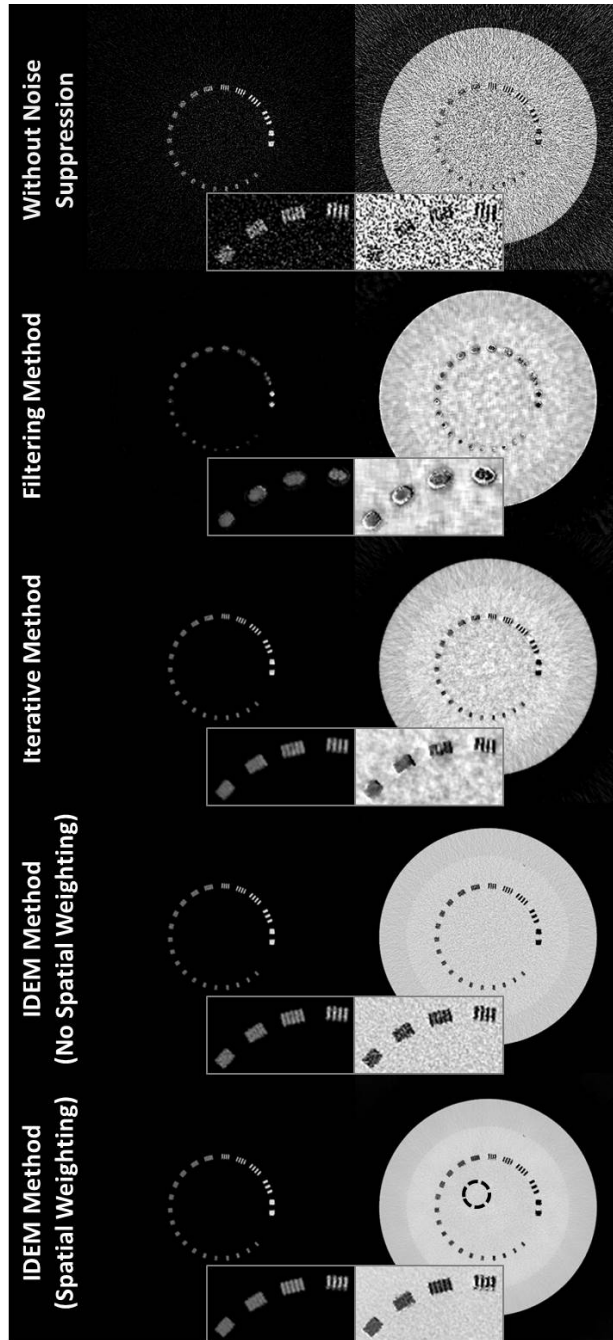
Figure 2.6: Decomposed images of the line-pair slice of Catphan©600 phantom. Within each image set, the "bone" image precedes the "tissue" image. The inserts are zoom-in images of line pairs with spatial frequencies from 5 to 8 line pairs/cm. In the bottom-right image, the dashed circle indicates the ROI used for the mean and noise STD calculations shown in Table 2.1. The tuning parameters of the IDEM algorithm, (ϵ, δ), are set to $(1.27, 3.17)$ when spatial weighting is not implemented and $(1.32, 3.77)$ with spatial weighting employed. Display windows are [0.1 1.2].

It is worth noting that, although the decomposed images produced by the different noise suppression algorithms have approximately the same noise STD, the image quality differs greatly. This phenomenon is due to different noise correlation characteristics in these images. Fig. 2.7 shows the NPS measured within an ROI of 100 by 100 pixels centered in the CT and "tissue" images. It is seen that decomposition without noise suppression and the IDEM method without spatial weighting both maintain the overall structure of NPS in the original CT image. The filtering method and the iterative method, however, preferentially suppress high frequency noise, which alters the texture of the decomposed images. Similar performance on NPS is expected with other existing methods, as long as they suppress noise by reducing spatial variations of neighboring signals. When the IDEM method uses spatial weighting, the same type of NPS degradation appears (i.e., increase of NPS signals in the low-frequency region). The overall NPS performance, however, is still superior to those of the filtering or iterative methods as shown in Fig. 2.7.
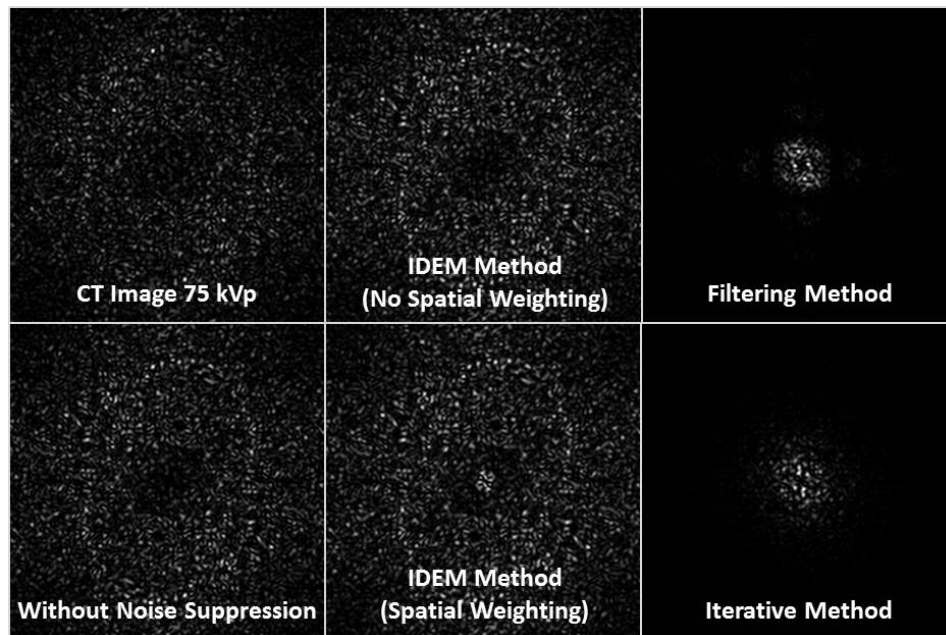

Figure 2.7: Measured NPS on the 75 kVp CT image and the "tissue" images generated by different algorithms. Zero frequency is at the center of NPS images. Each NPS was produced from an ROI of 100 by 100 pixels centered in the respective image. The images are displayed with a window of [min max].

2.3.2 Catphan Study on Electron Density Accuracy

In this study, we aim to investigate possible adverse effects of the IDEM method on decomposition accuracy. Fig. 2.1a shows the low and high energy CT images from a slice of Catphan©600 phantom that contains several contrast rods. Using these images, we perform material decomposition via Eqn. (2.3) with no noise suppression and the IDEM method. The decomposed images are shown in Fig. 2.8. For these results, the proposed search algorithm for minimum entropy refines the angle of the optimal axis for noise suppression obtained through SVD from $73.13°$ to $72.21°$. Algorithm parameters are tuned for strong noise suppression with noise STD reduction by a factor of around 13 on decomposed images. Fine structures are still well preserved in the images obtained by the proposed noise suppression. By applying Eqn. (2.17), electron densities are calculated from the decomposed images, generating the images shown in the third column of Fig. 2.8. The measured electron densities for different contrast rod materials and the RMS of the average percent errors for different materials are summarized in Table 2.2. An RMS error of 1.61% is observed on the results with direct decomposition and no noise suppression, mainly due to the uncorrected beam hardening artifacts in the CT images and possibly limitations of a linear DECT approach to electron density measurements. The IDEM method introduces an extra small bias of 1.16% and 0.38% when implemented without and with spatial weighting, respectively. These results indicate that our method substantially reduces the noise in decomposed images with limited effect on decomposition accuracy and that the inclusion of spatial weighting reduces most bias errors. It is worth emphasizing that, to fully investigate the capability of the IDEM algorithm on noise suppression, we have tuned algorithm parameters for very strong noise suppression. If less strong noise suppression is implemented, the bias from our algorithm is expected to decrease.
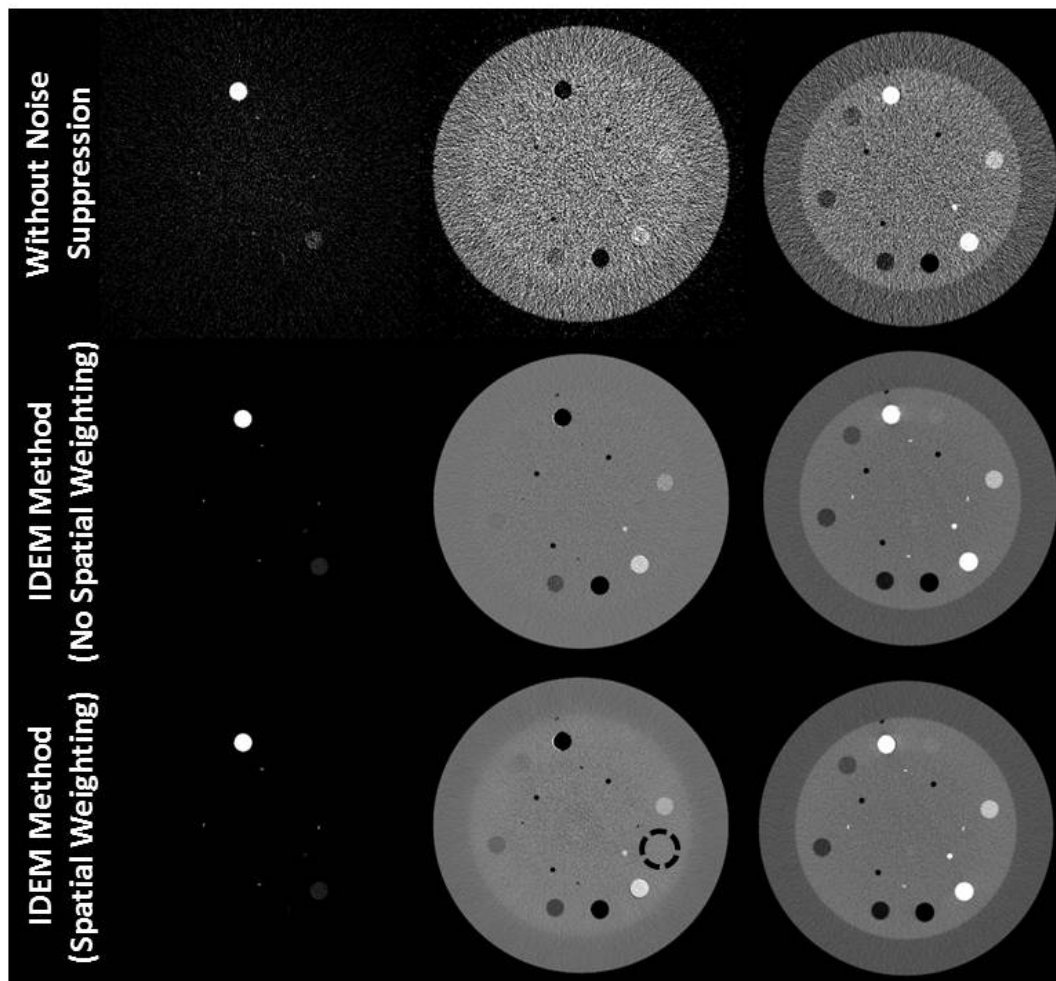
Figure 2.8: Decomposed and electron density images of the contrast-rod slice of the Catphan©600 phantom. The first, second, and third columns are "bone," "tissue," and electron density images, respectively. In the "tissue" image of the last row, the dashed circle indicates the ROI used for noise STD calculations. The tuning parameters of the IDEM algorithm, (ϵ, δ), are set to $(0.57, 3.00)$ when spatial weighting is not implemented and $(0.80, 4.90)$ with spatial weighting employed. Display windows are [0.1 0.7] for the bone images, [0.6 1.4] for the tissue images, and [2.75 5] $\times 10^{23}$ e/cm^3 for the electron density images.

Table 2.2: Electron densities (10^{23} e/cm^3) for the Catphan© contrast rod study. The last row is the root mean square of material percent errors.

	Reference Values	Without Noise Suppression	IDEM Method (NSW)	IDEM Method (SW)
Teflon	6.24	6.04 ± 0.8	5.99 ± 0.2	6.03 ± 0.2
PMP	2.85	2.89 ± 0.6	2.92 ± 0.2	2.89 ± 0.1
LDPE	3.16	3.19 ± 0.6	3.25 ± 0.1	3.21 ± 0.2
Polystyrene	3.34	3.38 ± 0.7	3.40 ± 0.1	3.40 ± 0.1
Aluminum	7.83	7.87 ± 0.9	7.95 ± 0.2	7.92 ± 0.2
Acrylic	3.83	3.84 ± 0.7	3.78 ± 0.1	3.81 ± 0.1
Delrin	4.56	4.49 ± 0.6	4.38 ± 0.2	4.45 ± 0.1
RMS of % Errors	N/A	$\mathbf{1.61 \pm 16.15\%}$	$\mathbf{2.77 \pm 3.28\%}$	$\mathbf{1.99 \pm 2.78\%}$

2.3.3   Anthropomorphic Head Phantom Study

The CT images and the decomposed images of the anthropomorphic head phantom are shown in Figs. 2.9 and 2.10, respectively. Prior to noise suppression, the IDEM method refines the angle of the optimal axis from $67.40°$ to $66.52°$. Table 2.3 summarizes the mean pixel values and noise STDs within an ROI (indicated by the dashed circle in Fig. 2.10) of the decomposed images. Once again, we tune the algorithm parameters so that all the methods achieve similar levels of noise suppression. Method performances similar to those in the Catphan©600 studies are observed in the image comparison. All three methods reduce the average noise STD by a factor of about 24 on the decomposed images. The entropy minimization based methods best preserve the image spatial resolution, which is obvious on the image comparison of sinus area shown in Fig. 2.11. The fine, intricate structures shown in the initial CT images are still clearly differentiable on the images obtained by the IDEM method, while other approaches generate image blur. Furthermore, since our method has less effect on the image NPS, the resultant image quality appears more natural. The images obtained by other methods contain noise artifacts due to the increased noise

correlation between neighboring pixels. By comparing the results with and without the proposed noise suppression in Table 2.3, we find that the IDEM algorithm with no spatial weighting introduces small bias on the decomposed material images and this small bias is effectively removed by the proposed spatial weighting scheme. In Fig. 2.10, it is interesting to note that the reduced image bias achieved by spatial weighting causes the images to match more closely the mean values of the images without noise suppression, which contain non-uniform beam hardening artifacts. As a result, the decomposed material images by the IDEM method with spatial weighting appear less uniform than those without spatial weighting.
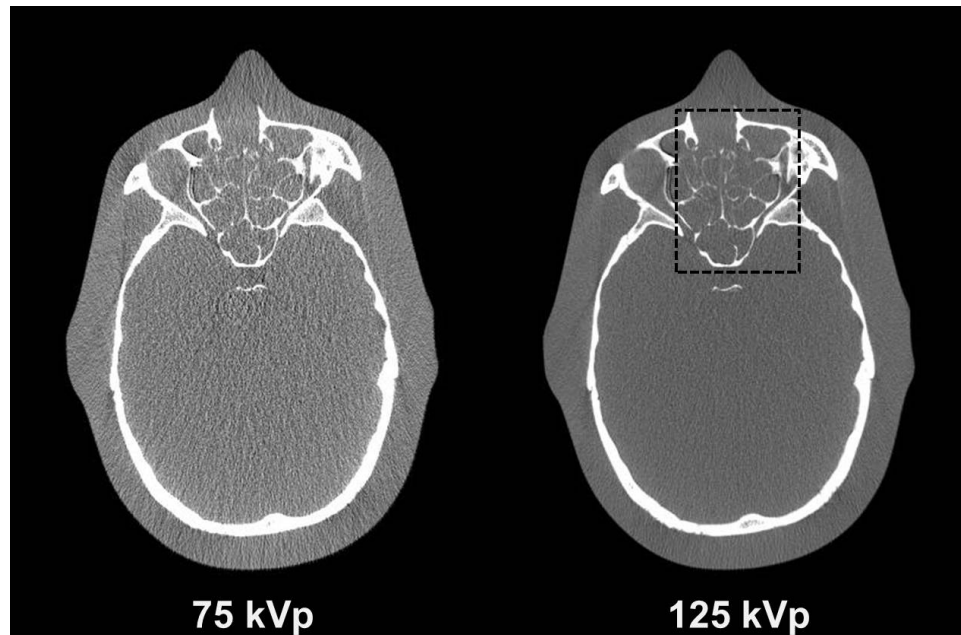
Figure 2.9: Low and high energy CT images of the anthropomorphic head phantom. The dashed box in the 125 kVp image indicates the location of the zoom-in images shown in Fig. 2.11 relative to the complete image. Display windows are [-500 1000] HU.

2.3.4   Patient Study

CT and decomposed images of a patient's head are shown in Figs. 2.12 and 2.13, respectively. Prior to noise suppression, the IDEM method refines the angle of the optimal axis
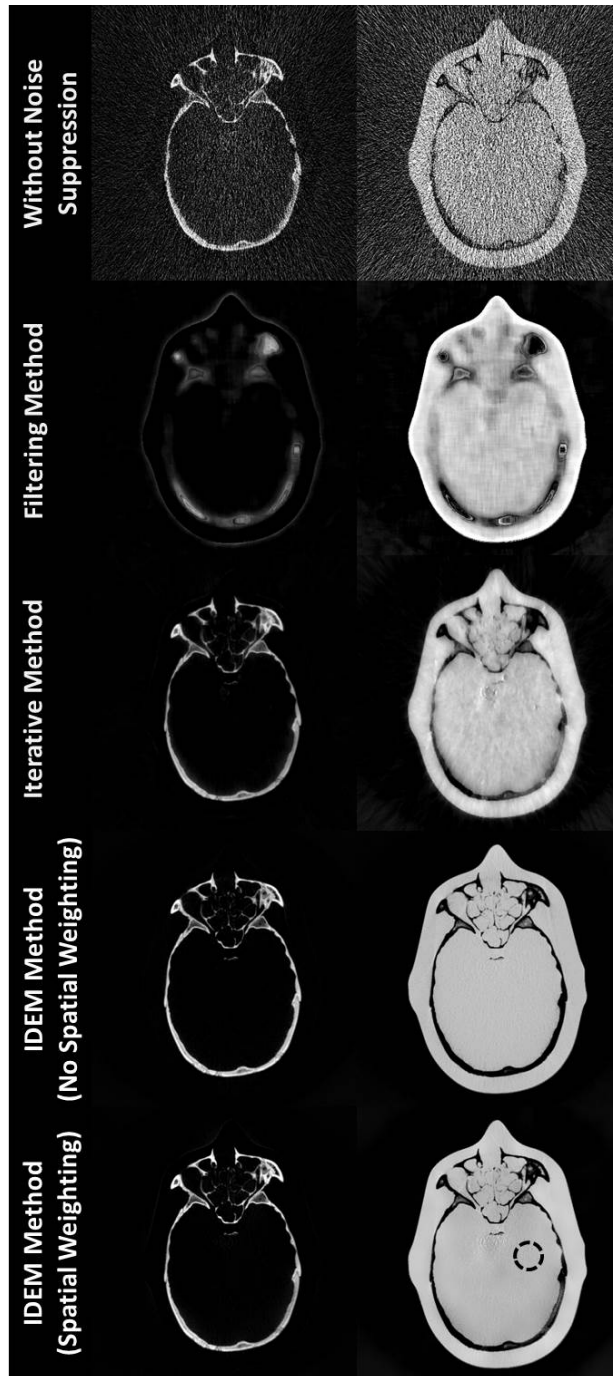
Figure 2.10: Decomposed images of the anthropomorphic head phantom. Within each im-age set, the "bone" image precedes "tissue" image. In the bottom-right image, the dashed circle indicates the location of the ROI used for mean and noise STD calculations. The tun-ing parameters of the IDEM algorithm, (ϵ, δ), are set to $(0.72, 9.37)$ when spatial weighting is not implemented and $(1.00, 9.07)$ with spatial weighting employed. Display windows are [0.01 1.4].
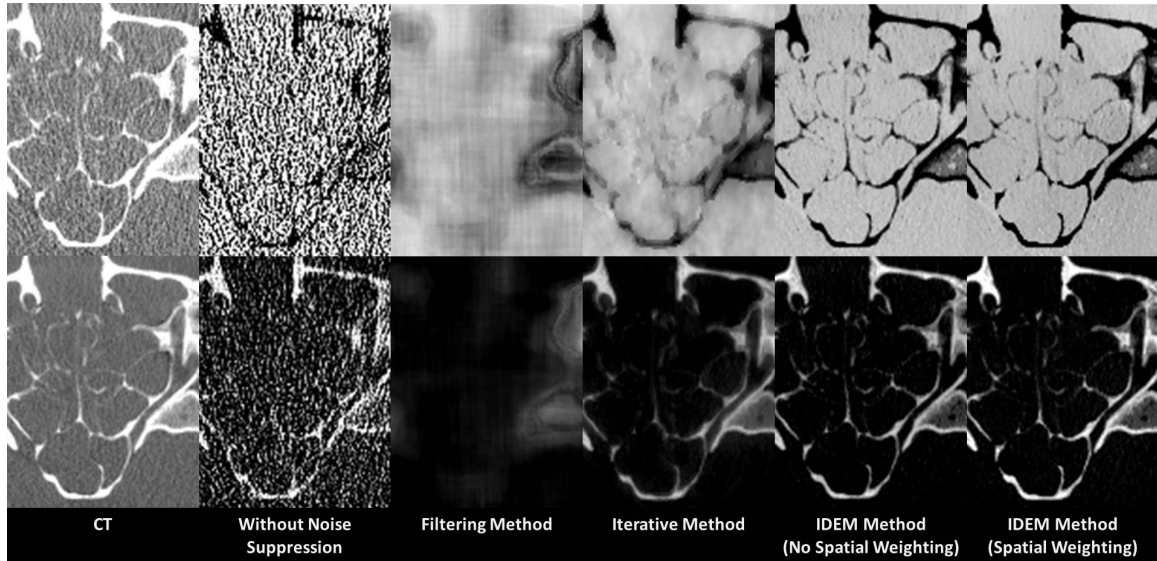
Figure 2.11: Zoom-in images of the anthropomorphic head phantom within the area indicated by the dashed box in Fig 2.9. The top-left and bottom-left images are 75 kVp and 125 kVp CT images, respectively. Within each set of decomposed images, the "tissue" image is shown in the top row, and the "bone" image is shown in the bottom row. CT images have a display window of [-500 1000] HU. Basis material images have a display window of [0.01 1.4].

Table 2.3: Mean and STD values within the ROI (indicated by the dashed circle in Fig. 2.10) of the decomposed images on the anthropomorphic head phantom.

	"Bone" Image	"Tissue" Image
Without Noise Suppression	0.00 ± 0.6	1.00 ± 2
Filtering Method	-0.04 ± 0.03	1.10 ± 0.06
Iterative Method	-0.03 ± 0.03	1.07 ± 0.05
IDEM Method (NSW)	-0.02 ± 0.04	1.05 ± 0.04
IDEM Method (SW)	0.00 ± 0.04	1.00 ± 0.04

from $68.90°$ to $64.60°$. Table 2.4 summarizes the mean pixel values and noise STDs within an ROI (indicated by the dashed circle in Fig. 2.13) of the decomposed images. Once again, we tune the algorithm parameters so that all the methods achieve similar levels of noise suppression. The results of this study are consistent with those of the phantom studies. All three methods reduce the average noise STD by a factor of about 9 on the decomposed images. The entropy minimization based methods best preserve image spatial resolution, which is evident in both the "tissue" and "bone" images of Fig. 2.13 and clearly depicted by the zoom-in "tissue" images of Fig. 2.14. Iodine-filled blood vessels and bony structures, such as the mandible, are well preserved on IDEM images while other approaches generate image blur and alter NPS, diminishing the natural appearance of their images. Note, the zoom-in "tissue" images also illustrate the respective merits of the IDEM method without and with spatial weighting. Without spatial weighting, there is greater definition between soft tissues while spatial weighting provides stronger delineation of blood vessels. By comparing the results in Table 2.4, we see that both IDEM algorithms outperform the other techniques with respect to induced bias and demonstrate comparable results to one another. Although the IDEM method does induce a slight bias on both decomposed images when spatial weighting is not employed, implementation of spatial weighting reduces the bias on the "tissue" image to a negligible level.

2.4 Discussion and Conclusions

Noise amplification has been a well-known issue of DECT since its invention [27, 28]. In this chapter, we propose a new algorithm for improving DECT image quality by reducing the noise on decomposed images, namely the IDEM method. Our approach is distinct from other existing methods in that it processes decomposed images by minimizing the signal entropy, instead of reducing the signal variation between neighboring pixels. As a consequence, image spatial resolution is preserved with limited effect on NPS even if
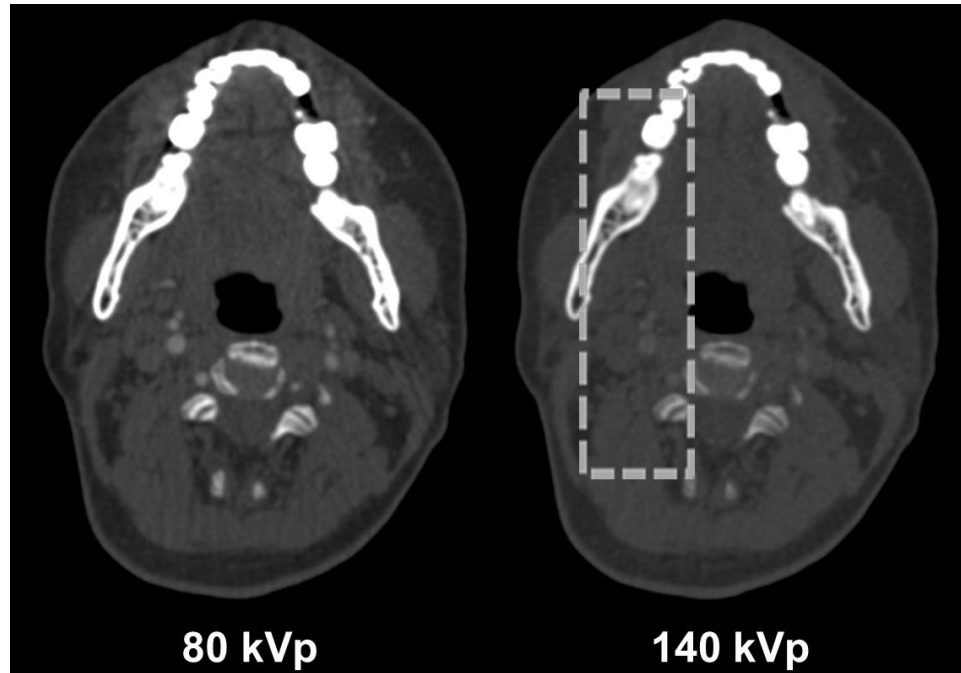
Figure 2.12: Low and high energy CT images of patient. The dashed box in the 140 kVp image indicates the location of the zoom-in images shown in Fig. 2.14 relative to the complete image. Display windows are [-300 1200] HU.
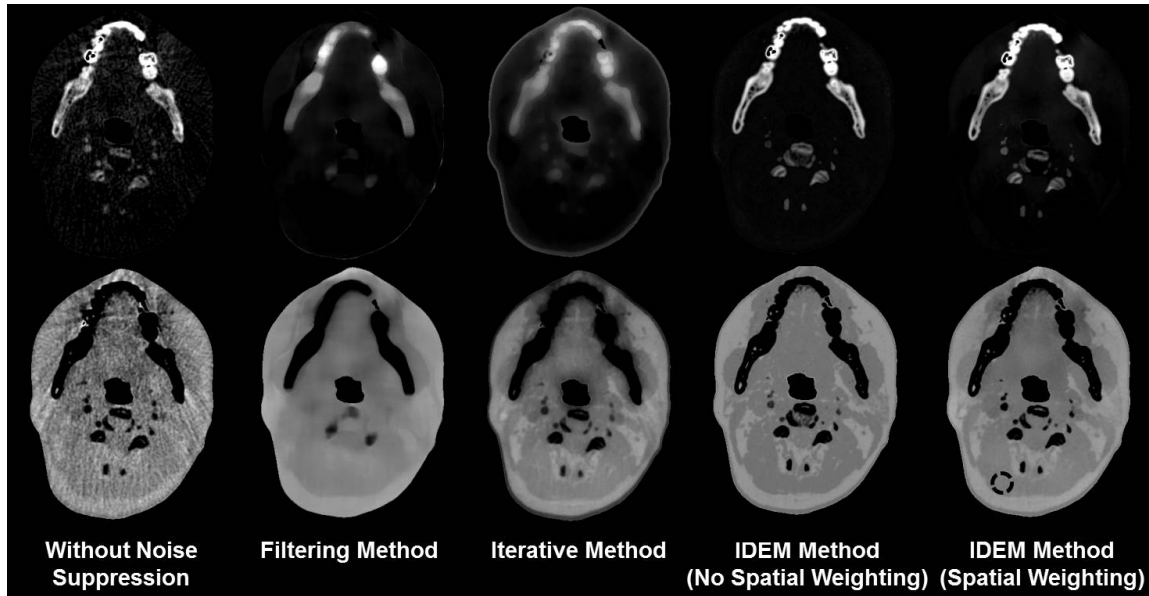
Figure 2.13: Patient decomposed images. The top row contains "bone" images while the bottom row shows "tissue" images. In the bottom-right image, the dashed circle indicates the location of the ROI used for mean and noise STD calculations. The tuning parameters of the IDEM algorithm, (ϵ, δ), are set to $(0.79, 43.5)$ when spatial weighting is not implemented and $(1.19, 30.0)$ with spatial weighting employed. Display windows for the "bone" and "tissue" images are [0.01 1.2] and [0.8 1.2], respectively.
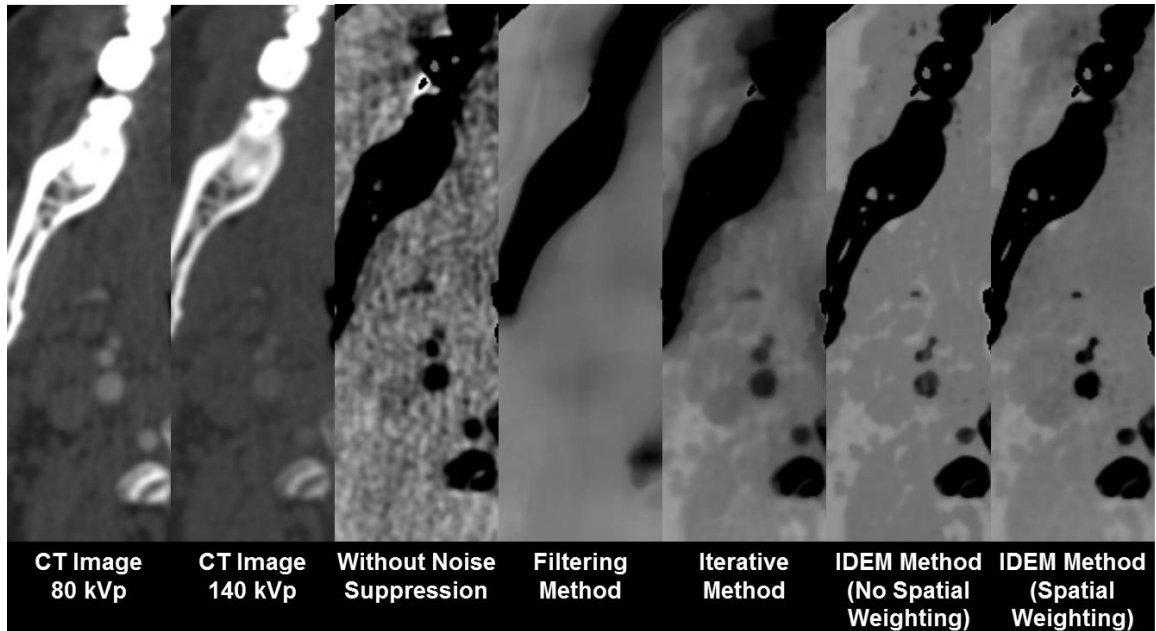
Figure 2.14: Zoom-in images of patient images within the area indicated by the dashed box in Fig 2.12. The first two images are the CT images. The remaining images are "tissue" images. CT images have a display window of [-300 1200] HU. "Tissue" images have a display window of [0.8 1.2].

Table 2.4: Mean and STD within the ROI (indicated by the dashed circle in Fig. 2.13) of patient basis material images.

	"Bone" Image	"Tissue" Image
Without Noise Suppression	0.02 ± 0.05	0.99 ± 0.03
Filtering Method	-0.01 ± 0.006	1.00 ± 0.004
Iterative Method	-0.01 ± 0.004	1.00 ± 0.006
IDEM Method (NSW)	0.03 ± 0.007	0.98 ± 0.003
IDEM Method (SW)	0.00 ± 0.005	0.99 ± 0.004

strong noise suppression is applied. This appealing feature is supported by the presented phantom and patient studies.

Since this method is applied on decomposed material images at the post-processing stage with a flexible framework, it can be combined with existing methods for further enhanced noise suppression. More evaluation studies and algorithmic improvements are of high interest in our future research to make the entropy minimization based method practical in clinical rooms. The IDEM method achieves material differentiation in a 2D decomposition space by using a brute-force searching scheme to orient an axis such that the projection of all data points onto that axis has minimal entropy. If the step size of the search is too large or too few histogram bins are used in the entropy calculation, the algorithm could potentially find a suboptimal angle. In addition to further optimizing the IDEM algorithm parameters for method stability on various DECT data, we will look into other entropy minimization algorithms for improved computational efficiency [41]. Future work will also include extensive investigations on material decomposition accuracy which go beyond the electron density calculations presented in this paper and will assess the IDEM method's performance on specific clinical tasks.

Also, in the presented studies we used the same parameter values for noise suppression at different pixel locations, which assumes that noise is stationary on CT images. We will improve the algorithm by using different algorithm parameters for different pixels based on the estimated variance of non-stationary noise. The noise variance maps of the initial CT images can be estimated by existing algorithms, for example, an FBP-based algorithm previously developed by our group [42]. When applying the entropy minimization based method on volumetric DECT data, the computation time of the IDEM method greatly prolongs. Since the entropy minimization algorithm processes each image pixel/voxel independently, a structure compatible for parallel computing, we will implement the algorithm on a graphics-processing-unit (GPU) based workstation for acceleration [43].

In conclusion, we propose a novel method utilizing entropy minimization within a 2D

transformation space for noise suppression on decomposed images of DECT, i.e., IDEM. Distinct from other noise suppression techniques, the IDEM method does not estimate and suppress noise based on spatial variations of signals and thus has potential to better preserve image spatial resolution and NPS. In Catphan©600 studies, the IDEM method reduces noise STD on decomposed images by a factor of around 13 while limiting the induced error in electron density calculations to 1.16% and 0.38% without and with spatial weighting, respectively. The method reduces the noise STDs on decomposed images of an anthropomorphic head phantom by a factor of at least one order of magnitude. Similar performance is also seen on patient images. In all presented studies, the proposed method retains greater spatial resolution than a conventional filtering method and a recently developed iterative method at the same level of noise suppression, while largely preserving the NPS of the initial CT images.

CHAPTER 3

SINGLE-SCAN DUAL-ENERGY CT THROUGH PRIMARY MODULATION

3.1 Introduction

To acquire projection data with two different x-ray spectra, DECT can be carried out on a standard CT scanner with two full CT scans of different kVp values. However, the utility of this technique is limited by patient motion between dataset acquisitions which leads to geometric differences between high and low energy datasets and ultimately to artifacts in decomposed images. Using hardware components (i.e., dual sources [1], a fast kVp-switching x-ray source [1], or a dual-layer detector [1]), costly specialized scanners perform DECT imaging with scan time and dose comparable to that of a standard CT scan. These systems, however, are still not ubiquitously available in hospitals.

We aim to develop a practical solution of single-scan DECT imaging on a standard CT scanner without upgrades of major hardware components. Our previous work has shown that beam filtration achieves sufficient spectral separation for DECT imaging and that single-scan DECT is feasible when redundant projection rays are available [44]. In this chapter, we extend our method to single-scan DECT without the requirement of projection redundancy. Small beam filters are distributed across the imaging field to acquire sparse projection data with effective high and low-energy spectra. An iterative algorithm is proposed for image reconstruction and material decomposition from sparse projection data. Since the geometry of beam filters is the same as that of the primary modulation technique for scatter correction [45, 46, 47, 48], the proposed method is referred to as primary modulation based DECT (PM-DECT). We demonstrate the feasibility of PM-DECT on a flat-panel based tabletop CT system. Method performance is evaluated with respect to spatial resolution and decomposition accuracy via phantom studies.

3.2 Method

3.2.1 System Geometry for PM-DECT

Figure 3.1 shows the system geometry using primary modulation. By inserting an attenuation sheet with a spatially-varying pattern (primary modulator) between the x-ray source and the imaged object, we selectively harden the x-ray beam at specific detector pixel locations, represented by the shaded regions in Fig. 3.1. This increases the average x-ray energy at specific detector locations and thereby enables the proposed method to simultaneously acquire high and low energy data at each projection angle during a single scan. In this work, we utilized a 1D primary beam modulator to simplify manufacturing of the modulator as well as the experimental setup. As shown in Fig. 3.1, the strips of filtering material are oriented parallel to the axis of rotation producing beam modulation in each image slice. (For additional details about beam hardening, please refer to Appendix A.)
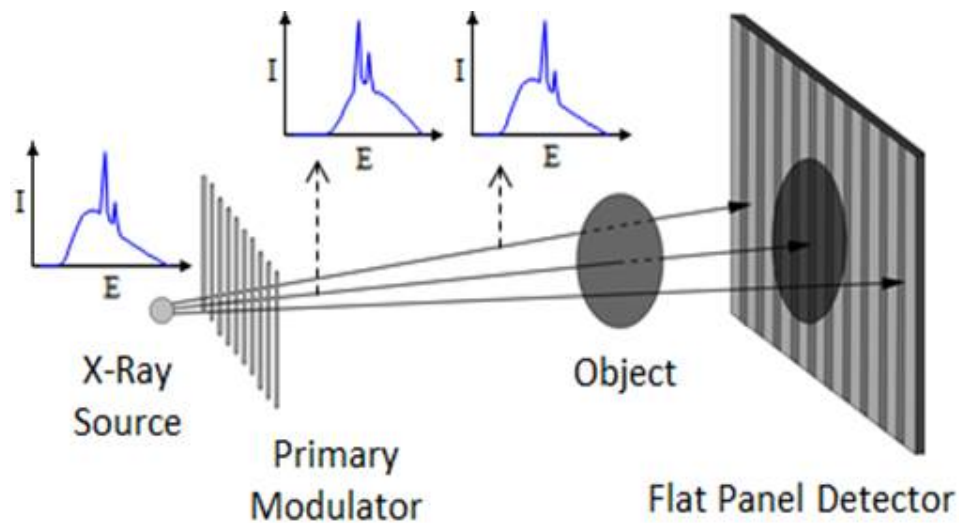

Figure 3.1: CT system geometry for PM-DECT. From left to right the plots depict the photon spectrum at three different locations: 1) upon exiting the x-ray tube, 2) after passing through the primary modulator with filtration, and 3) after passing through the primary modulator without filtration.

3.2.2 Iterative Image Reconstruction and Material Decomposition

In PM-DECT, we first separate filtered and unfiltered projection data and reconstruct high and low-energy CT images. Similar to dual-source DECT [1, 9, 24], PM-DECT does not measure identical projection rays using different x-ray source spectra. We therefore use image-domain decomposition in PM-DECT to generate basis material images.

Each filter of the primary modulator covers tens of pixels on the detector, and due to the limitation of finite focal-spot size, the filters need to be separated by at least that distance to permit measurements outside the penumbra region. As such, the geometry of PM-DECT yields very sparse high and low-energy projection data that pose particular challenges in the signal processing. Standard FBP reconstruction on sparse projection data generates CT images with severe artifacts and resolution loss. Material decomposition exacerbates the problem due to its high sensitivity to errors within CT images [25, 26, 49].

As described in Chapter 2, image-domain decomposition assumes a linear relationship between the CT and basis material images for each pixel location, i.e., $\overrightarrow{\mu} = A\overrightarrow{x}$. Solving for $\overrightarrow{x}$ yields the following equation for image-domain decomposition:

$$\overrightarrow{x} = A^{-1}\overrightarrow{\mu} \tag{3.1}$$

where

$$A^{-1} = \begin{bmatrix} a & b \\ c & d \end{bmatrix} = \frac{1}{\det(A)} \begin{bmatrix} \mu_{2l} & -\mu_{2h} \\ -\mu_{1l} & \mu_{1h} \end{bmatrix}. \tag{3.2}$$

In practice of DECT, A^{-1} typically has a condition number much greater than 10, leading to significant error or noise amplification on basis material images [25, 26, 49].

Recently, we have proposed a few iterative algorithms to improve the accuracy of CT reconstruction and DECT material decomposition [25, 26, 31, 43, 50, 51, 52]. For example, the compressed sensing based algorithm successfully reconstructs images from limited projection data [31, 43]. This algorithm has been improved for enhanced noise suppression

performance in DECT [25]. By combining the reconstruction and decomposition into an iterative process, we simultaneously use all of the available data and fully explore the noise statistical properties of decomposed images during CT reconstruction to generate high resolution noise-suppressed decomposed images. A similarity-based iterative algorithm further recovers image spatial resolution of DECT when projection data are extremely sparse, by exploiting redundant structural information [50]. In this chapter, we combine the above three techniques for PM-DECT.

The framework of image reconstruction and material decomposition for PM-DECT takes the following form of optimization:

$$
\begin{aligned}
[\overrightarrow{\mu_h}^*, \overrightarrow{\mu_l}^*] \;=\; \min\Bigg[& \|(M_l\overrightarrow{\mu_l} - \overrightarrow{s_l})\|_2^2 + \eta\|M_h\overrightarrow{\mu_h} - \overrightarrow{s_h}\|_2^2 \\
& + \alpha_1 R(a\overrightarrow{\mu_h} + b\overrightarrow{\mu_l}) + \alpha_2 R(c\overrightarrow{\mu_h} + d\overrightarrow{\mu_l}) \\
& + \beta_1 R(\overrightarrow{\mu_h}) + \beta_2 R(\overrightarrow{\mu_l}) \Bigg] \\
& \text{s.t. } \overrightarrow{\mu_h} \geq 0, \overrightarrow{\mu_l} \geq 0 \,.
\end{aligned}
\tag{3.3}
$$

In Eqn. (3.3), $\overrightarrow{s_h}$ and $\overrightarrow{s_l}$ represent portions of the modulated sinogram containing high and low-energy data, respectively. $\overrightarrow{s_h}$ and $\overrightarrow{s_l}$ are extracted from the modulated sinogram at the appropriate detector-pixel locations determined by thresholding of the modulated flat field. M_h and M_l are forward-projection matrices for the high and low-energy detector pixels, respectively. They are generated using Siddon's ray tracing algorithm [53]. η is the ratio of low energy to high energy projection data. Including η places equal importance on the high and low energy datasets even if the two datasets are disproportionate in size. R is the image regularization function performing an improved version of similarity-based regularization [50] (see detailed discussion below) while α_1, α_2, β_1, and β_2 are the weighting factors on the regularization terms. The first four terms of the optimization objective in Eqn. (3.3) combine iterative CT reconstruction with DECT material decomposition for enhanced noise suppression as shown in Ref. [25]. The inclusion of the last two terms further

improves the accuracy of PM-DECT. The optimization is solved efficiently by gradient projection with an adaptive Barzilai-Borwein (GP-BB) step-size selection scheme which was proposed in our recent publications [31, 43].

Another critical aspect to the proposed algorithm's design is the regularization term R, which is defined as:

$$R\left(\overrightarrow{f}\right) = \frac{1}{2}\|\nabla(I-W)\overrightarrow{f}\|_1 + \frac{\xi}{2}\|\nabla(I-W_e)diag(\overrightarrow{\nu})\overrightarrow{f}\|_1 \qquad (3.4)$$

where I is an identity matrix and $\overrightarrow{f}$ is the image. The first term of Eqn. (3.4) is similar to the previously proposed similarity-based regularization [50], which reduces the signal variation of similar pixels, except that we divide the entire set of pixels into two groups and compute the similarity separately. The matrix W quantifies the level of similarity between each pair of pixels, calculated as:

$$W(i,j) = \begin{cases} \dfrac{(1-\overrightarrow{\nu}(j))\cdot\exp\left[-\left(\frac{\overrightarrow{\mu_r}(j)-\overrightarrow{\mu_r}(i)}{h}\right)^2\right]}{\sum\limits_{j\in\Omega_i}(1-\overrightarrow{\nu}(j))\cdot\exp\left[-\left(\frac{\overrightarrow{\mu_r}(j)-\overrightarrow{\mu_r}(i)}{h}\right)^2\right]} & \text{if } \begin{matrix} j\in\Omega_i \text{ \&} \\ \overrightarrow{\nu}(i)=0 \end{matrix} \\[4em] \dfrac{\overrightarrow{\nu}(j)\cdot\exp\left[-\left(\frac{\overrightarrow{\mu_r}(j)-\overrightarrow{\mu_r}(i)}{h}\right)^2\right]}{\sum\limits_{j\in\Omega_i}\overrightarrow{\nu}(j)\cdot\exp\left[-\left(\frac{\overrightarrow{\mu_r}(j)-\overrightarrow{\mu_r}(i)}{h}\right)^2\right]} & \text{if } \begin{matrix} j\in\Omega_i \text{ \&} \\ \overrightarrow{\nu}(i)=1 \end{matrix} \\[4em] 0 & \text{otherwise} \end{cases} \qquad (3.5)$$

We reconstruct a reference image, $\overrightarrow{\mu_r}$, from the modulated sinogram using FBP and ring correction algorithms. In Eqn. (3.5), h is the Gaussian kernel width (set as 0.0006 mm^{-1} in our studies) and Ω_i is a set of pixels around pixel i that have values within $\pm 3h$ of pixel i's value. As described in Ref. [50], we start the search for similar pixels within a G-by-G region of $\overrightarrow{\mu_r}$ centered on pixel i. The initial value of G is set as 15. If the number of pixels found is less than 200, the search continues with G doubled. This is repeated until there are 200 such pixels or the whole reference image is included. $\overrightarrow{\nu}$ is an indicator vector which separates pixels with few similar pixels from the reference image. $\overrightarrow{\nu}$ is assigned a value of

1 if the size of Ω_i is less than 25 at the G value of 15 and 0 otherwise. In Eqn. (3.5), the function $diag()$ transforms a vector into a diagonal matrix.

The second term of Eqn. (3.4) reduces the error of one particular pixel when it has very few similar pixels. The matrix W_e is computed as:

$$W_e(i,j) = \begin{cases} \dfrac{\exp\left[-(distance(j,i))^2\right]}{\sum\limits_{j} \exp\left[-(distance(j,i))^2\right]} & \text{if } \vec{\nu}(i)=1 \\[20pt] 0 & \text{otherwise} \end{cases} \tag{3.6}$$

where $distance()$ is a function that returns the geometric distance separating pixels i and j. Including the second term of Eqn. (3.4) is equivalent to additional spatial filtration which improves the accuracy and stability of PM-DECT. ξ is a tunable parameter controlling the relative strength of the spatial filtration compared to that of the similarity based regularization.

3.2.3 Implementation Details

The condition number of the decomposition matrix A determines the robustness of DECT decomposition. Larger values indicate an ill-conditioned process that is more sensitive to errors in $\vec{\mu}$, increasing degradation to image quality during decomposition [49]. From simulated spectra we can compute condition numbers for different modulator designs. Previous research on scatter correction via primary modulation has used a modulator constructed from copper with a thickness of 0.406 mm [46]. Fig. 3.2 shows the condition number for this modulator design using bone and water as basis materials. The modulator performs well for water-equivalent objects of low thicknesses, but as the modulated beam passes through greater lengths of water, condition numbers increase because the unfiltered portion of the beam is progressively hardened by the imaged object and spectral separation decreases.

In order to reduce condition number and boost decomposition robustness, we can in-

crease spectral separation through greater beam filtration. As depicted in Fig. 3.2, if we replace copper with the same thickness of molybdenum, the condition number drops by more than a factor of two for water-equivalent thickness greater than 20 cm. This suggests that replacing copper with molybdenum would lead to improved decomposition quality. Thus, we chose to create a primary modulator from molybdenum for the DECT studies presented in this chapter. The molybdenum primary modulator and its dimensions are displayed in Fig. 3.3. The modulator has a thickness of 0.381 mm, leading to a shift of 24 keV on the mean x-ray energy after modulator filtration.

We performed proof-of-concept phantom studies at the Georgia Institute of Technology on a tabletop CT system [37], the geometry of which matches that of the on-board imager system of a Varian radiation therapy machine. The x-ray tube (Varian RAD-94) has inherent filtration of 0.5 mm Al. Phantom data are acquired for 655 projection views using the
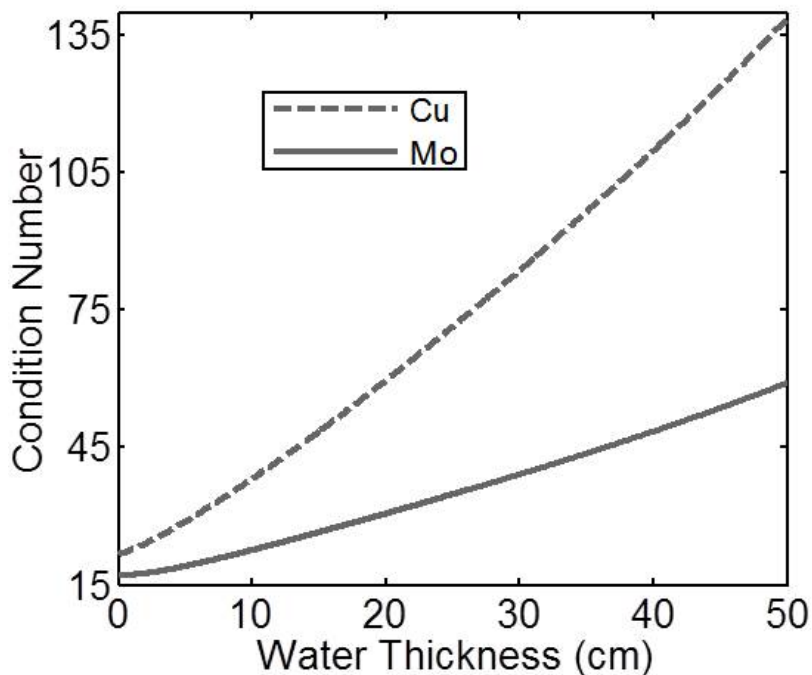
Figure 3.2: Decomposition matrix condition numbers calculated from simulations using bone and water as basis materials. The tube potential is set to 125 kVp for these simulations because 125 kVp provided the lowest condition numbers of the tube potentials available on our CT system.

molybdenum primary modulator, a tube potential of 125 kVp, and a tube current of 80 mA.

In the proposed algorithm, i.e., Eqn. (3.3), η is set as the ratio of the number of low-energy pixels over high-energy pixels. a, b, c, and d are determined by the selected basis materials, as shown in Eqn. (3.2). In these studies, we used Teflon and polystyrene as basis materials for reconstruction. Note that after reconstruction is complete, one may generate decomposed images with any basis materials simply by inserting the reconstructed low and high-energy images and the desired decomposition matrix into Eqn. (3.1). To reduce the complexity of parameter tuning, we set $\alpha_1 = \beta_2 = 0$. Therefore, α_2, β_1, and ξ are the only parameters in the proposed algorithm that require empirical tuning. We find that the results are not very sensitive to the parameter values. α_2 and β_1 are held constant in all presented studies. ξ values are held nearly constant across the studies.
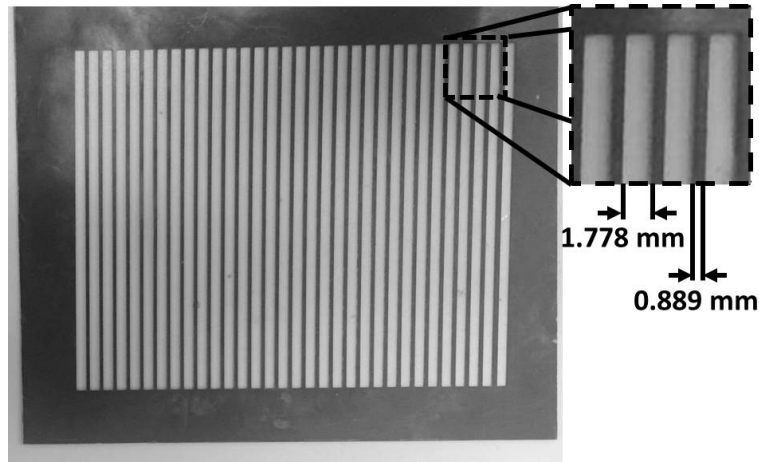

Figure 3.3: Primary beam modulator machined from a sheet of molybdenum 0.381 mm thick.

3.2.4 Evaluation

We have assessed method performance using an evaluation phantom, i.e., the Catphan©600 (The Phantom Laboratory: Salem, NY), and an anthropomorphic head phantom. To limit photon scatter, the phantoms were imaged with a narrowly opened collimator, i.e., a fan-

beam equivalent geometry. Sinograms were generated using four neighboring rows of detector pixels. High and low-energy CT images were reconstructed using the proposed PM-DECT framework, with an image size of 512 by 512 pixels and pixel resolution of 0.5 by 0.5 mm^2. Our algorithm for image reconstruction typically takes 20 hours using MATLAB on a 2.66 GHz CPU workstation.

One slice of the Catphan©600 phantom, which contains high contrast line pairs, was used to evaluate performance on spatial resolution. The line pairs with spatial frequency from 1 to 21 line pairs/cm are made of aluminum, surrounded by epoxy, a water-equivalent material. In the study, basis materials of aluminum and epoxy were chosen to create "bone" and "tissue" images, respectively. Spatial resolution of the proposed method was compared against the spatial resolution of an image reconstructed via FBP from an unmodulated CT scan.

A separate slice of the Catphan©600 phantom, which contains rods of different materials, was used to assess the accuracy of electron density measurements. We used polystyrene and Teflon as basis materials to create "tissue" and "bone" images, respectively. In this study, we compared PM-DECT's performance against that of a two-scan technique. In the latter, we scanned the phantom both with and without a solid molybdenum filter of 0.381 mm thickness and performed decomposition in the image domain after a standard CT reconstruction via FBP. As such, this method provides an accuracy benchmark for the selected modulator material and thickness. Contrast rods were used as ROIs for electron density measurement, calculated as:

$$\rho_e = \rho_{e,b} \cdot x_b + \rho_{e,t} \cdot x_t \tag{3.7}$$

where x_b and x_t are pixel values of decomposed bone and tissue images, and $\rho_{e,b}$ and $\rho_{e,t}$ are the electron densities of the bone and tissue materials, respectively. Note that the decomposed images are unitless and indicate the normalized densities of equivalent basis

materials contained inside one pixel. For each rod, the average percent error of associated pixels was determined using the equation:

$$E(\%) = \left(\frac{\overline{\rho_e} - \rho_e^{ref}}{\rho_e^{ref}} \right) \times 100\% \qquad (3.8)$$

where ρ_e^{ref} is the true electron density of a rod, which is provided in the Catphan©600 phantom's user manual, and $\overline{\rho_e}$ is the mean value of measured electron density inside the rod. The accuracy of our method as compared to that achieved without modulation was assessed using the root-mean-square (RMS) of the $E(\%)$ of all the rods.

The head phantom was used for comprehensive evaluations on an object with complicated structures. The head phantom is composed of epoxy mimicking soft tissue and a calcium compound mimicking bone. Note that, the calcium compound has a spatially varying density, producing a greater challenge during similarity matrix calculations. The calcium compound ("bone") and epoxy ("tissue") were chosen as basis materials in this study.

3.3 Results

3.3.1 Catphan Study on Spatial Resolution

Figure 3.4 shows images of the line-pair slice of Catphan©600 phantom produced via PM-DECT. An image generated from a CT scan without beam modulation is also presented for comparison. The low and high-energy images displayed in Fig. 3.4 were generated from a single scan using the modulator shown in Fig. 3.3. The zoom-in images of line-pairs shown in Fig. 3.5 illustrate that the high and low-energy images retain nearly the same spatial resolution as a conventional CT image even though these PM-DECT images were each reconstructed from limited projection data. The decomposed images in Figs. 3.4 and 3.5 show a high level of uniformity and the retention of spatial resolution.
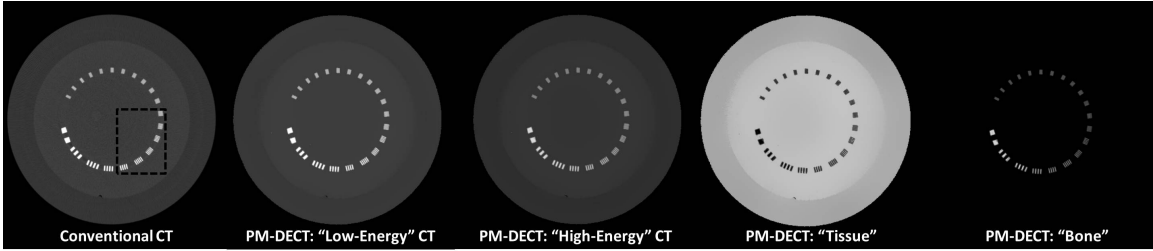
Figure 3.4: CT and decomposed images of the line-pair slice of Catphan©600 phantom. The first image is an FBP image produced from a conventional CT scan. The remaining images are those produced via PM-DECT. The "tissue" and "bone" images were generated from the "low-energy" and "high-energy" CT images. The dashed box indicates the locations from which the zoom-in images of Fig. 3.5 are taken. The display window for the CT images is [-500 2000] HU. The decomposed images have a display window of [0.2 1.3].
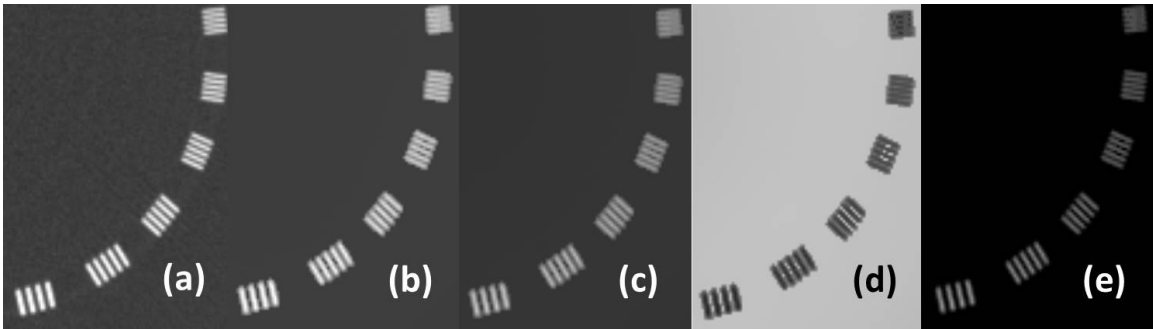

Figure 3.5: Zoom-in images of Catphan line pairs within the region depicted by the dashed box in Fig. 3.4. Images (a)-(e) are arranged in the same order as the parent images within Fig. 3.4. The line pairs represent spatial frequencies from 5 to 10 line pairs/cm. Display windows are the same as in Fig. 3.4.

3.3.2 Catphan Study on Electron Density Accuracy

In this section we investigate the accuracy of decomposed images through an analysis of the contrast-rod slice of the Catphan phantom. Fig. 3.6 displays a CT image generated via a conventional CT scan without modulation as well as CT and decomposed images generated through PM-DECT. The ability of PM-DECT to retain a high level of spatial resolution is demonstrated by the retention of most structures including the four wire ramps.

As stated in Section 3.2.4, decomposed images were generated from unfiltered and filtered CT scans to serve as a benchmark. These images are shown in Fig. 3.7. Within the ROI depicted by the dashed circle in Fig. 3.6, the mean attenuation coefficient of PM-

DECT's low-energy image differs from the unfiltered image by less than 0.1%. Despite being reconstructed from a dataset 10 times smaller than the filtered image, PM-DECT's high-energy image differs from the filtered image by only 1.1%. The close match to the benchmark values demonstrates the accuracy of the proposed reconstruction technique.

For the two-scan and PM-DECT techniques, electron densities were calculated using Eqn. 3.7 and are displayed in Table 3.1. The tabulated values of the two-scan technique indicate that a molybdenum filter of the tested thickness provides adequate spectral separation to generate accurate DECT results, i.e., with less than 0.50% error. PM-DECT, which produces decomposed images from a single CT scan, was able to achieve a limited error of 1.12%. However, we see that most of PM-DECT's error is due to the acrylic rod. Without the acrylic rod, PM-DECT outperforms the two-scan technique with RMS errors of 0.30±0.41% and 0.48±8.04%, respectively.

Figures 3.6 and 3.7 reveal the challenge of DECT material decomposition due to significant noise amplification. The decomposed images from the two-scan technique suffer from substantial SNR degradation. Compared with the conventional two-scan method, PM-DECT has prominent advantages by not only obtaining DECT images with much less noise but also jointly reconstructing high and low-energy CT images from one single CT scan.

Table 3.1: Electron densities (10^{23} e/cm^3) for the Catphan© contrast rod study. The last row is the root mean square of material percent errors.

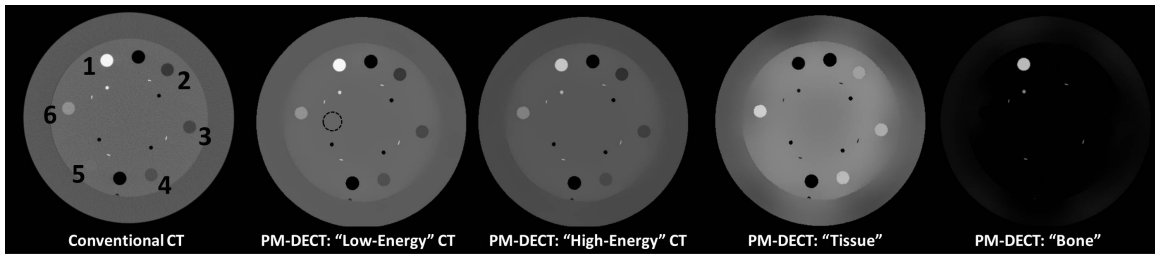|	Reference Values	Two-Scan Technique	PM-DECT
Teflon	6.24	6.24 ± 0.3	6.24 ± 0.0
PMP	2.85	2.85 ± 0.3	2.84 ± 0.0
LDPE	3.16	3.14 ± 0.3	3.17 ± 0.0
Polystyrene	3.34	3.34 ± 0.3	3.34 ± 0.0
Acrylic	3.83	3.82 ± 0.3	3.73 ± 0.0
Delrin	4.56	4.52 ± 0.3	4.58 ± 0.0
RMS of % Errors	**N/A**	$\mathbf{0.46 \pm 7.85\%}$	$\mathbf{1.12 \pm 0.37\%}$

Figure 3.6: CT and decomposed images of contrast-rod slice of Catphan©600 phantom. The first image was reconstructed via FBP from a conventional CT scan. The remaining images were produced via PM-DECT. The "tissue" and "bone" images were generated from the "low-energy" and "high-energy" CT images. The materials numbered in the conventional CT image are: [1] Teflon, [2] PMP, [3] LDPE, [4] Polystyrene, [5] acrylic, and [6] Delrin. The circle in the "low-energy" CT image locates a ROI used for pixel value analysis. Display windows are [-500 1000] HU for the CT images and [0.2 1.3] for the decomposed images.
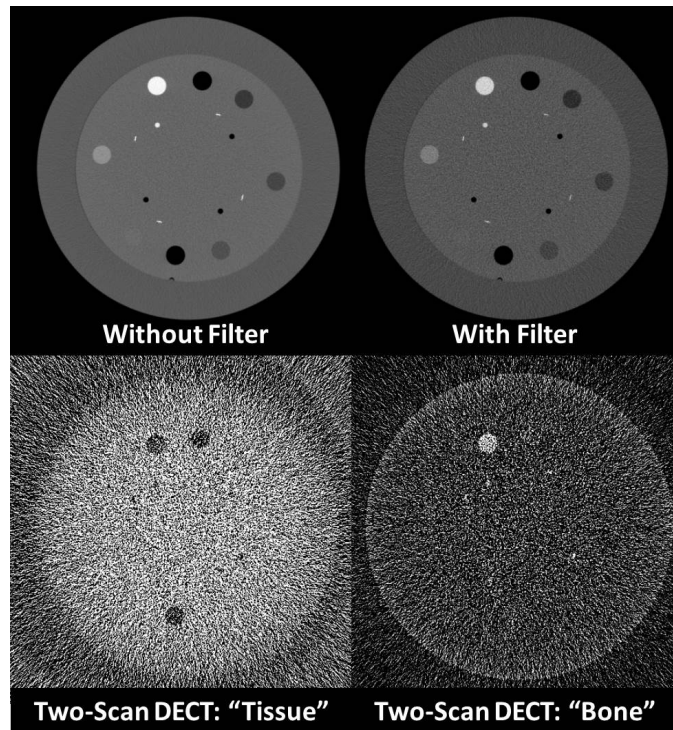

Figure 3.7: CT and decomposed images of the Catphan's contrast rod-slice for a two-scan technique. The first row contains CT images reconstructed via FBP from complete scan data acquired without and with beam filtration. The second row shows decomposed images generated from the FBP images. Display windows are [-500 1000] HU for the CT images and [0.2 1.3] for the decomposed images.

3.3.3 Anthropomorphic Head Phantom Study

CT images and decomposed images of the anthropomorphic head phantom are shown in Fig. 3.8. The results are consistent with those of the Catphan©600 studies. The PM-DECT's high and low-energy images have matching uniformity and spatial resolution compared against the conventional CT image. This is more apparent in the zoom-in images of the sinus region, which are shown in Fig. 3.9. Despite the spatial variations in material density within the head phantom, the proposed method is able to successfully separate the bone and tissue materials during decomposition, as illustrated in the decomposed images of Figs. 3.8 and 3.9. The decomposed images retain a very high level of spatial resolution and the appearance of fine structures. Slight nonuniformity is observed in the decomposed images around the periphery of the head. We believe that it is due to beam hardening artifacts from the highly attenuating bone structures. These artifacts are also visible in the conventional CT image and are not attributable to the proposed method.

It is worth noting that PM-DECT provides these DECT capabilities while retaining the ability to produce high-quality CT images. To this point, Fig. 3.10 shows two CT
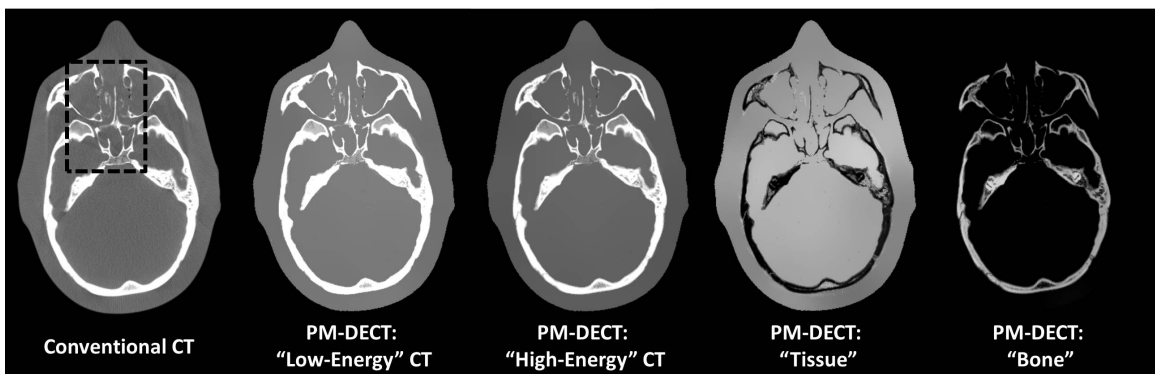
Figure 3.8: CT and decomposed images of the anthropomorphic head phantom. The first image was reconstructed via FBP from a conventional CT scan. The remaining images were produced via PM-DECT. The "tissue" and "bone" images were generated from the "low-energy" and "high-energy" CT images. The dashed box indicates the location of the zoom-in images that appear in Fig. 3.9. CT images have a display window of [-500 1000] HU. The "tissue" and "bone" images have display windows of [0.2 1.3] and [0.1 1.3], respectively.

Figure 3.9: Zoom-in images of the anthropomorphic head phantom within the area indicated by the dashed box in Fig. 3.8. Display windows are the same as in Fig. 3.8.

images: one produced from a single conventional scan without beam modulation and the other produced from a single PM-DECT scan. The latter was generated using FBP and ring correction algorithms. The quality of the PM-DECT image rivals that of the conventionally produced image. We see negligible artifacts and no loss of spatial resolution.

3.4 Discussion and Conclusions

DECT is fundamentally burdened by the need to acquire an additional dataset as compared to conventional CT, which restricts applications to specialized DECT scanners. In this chapter, we propose a new DECT technique referred to as PM-DECT, which uses primary modulation during data acquisition and an iterative algorithm for signal processing. PM-DECT is distinct from existing technologies by simultaneously collecting high and low-energy projection data during a single CT scan with limited hardware modifications to a conventional scanner. This removes the time-delay between high and low-energy data acquisitions in the two-scan DECT method or the need for additional equipment of expensive advanced CT scanners. Consequently, PM-DECT has the potential to liberate the applications of DECT from specialized scanners to other CT systems such as CBCT, which could greatly expand the scope of DECT in clinical implementations. In Catphan©600 studies, PM-DECT generates decomposed images while overcoming the challenge of noise amplification, achieving an almost complete retention of spatial resolution, and limiting error
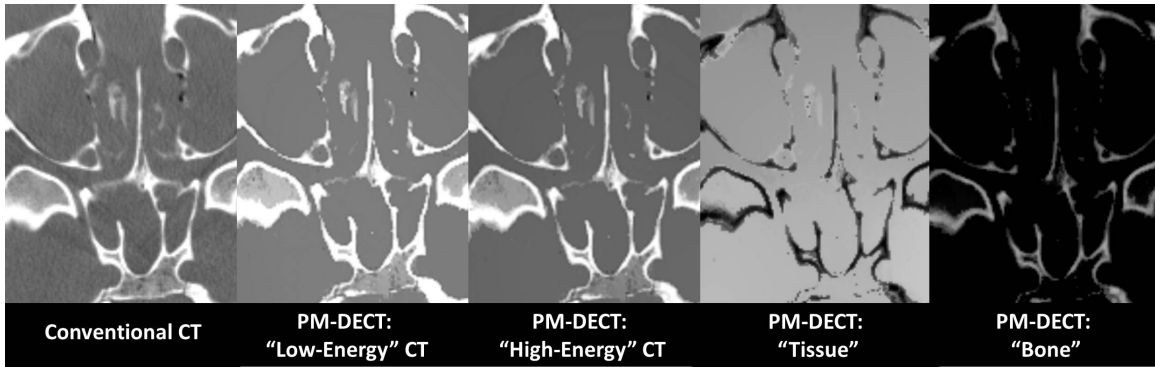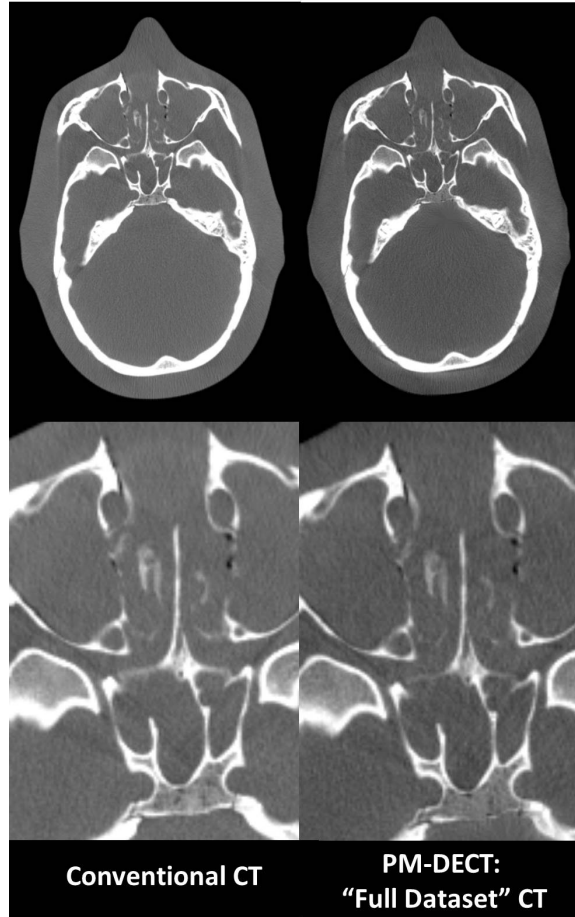
Figure 3.10: CT images of the anthropomorphic head phantom. From left to right, the first row contains an image reconstructed via FBP from a conventional CT scan and an image reconstructed via FBP using the complete set of PM-DECT projection data. The second row presents zoom-in images of the sinus regions. Display windows are [-500 1000] HU.

in electron density calculations to 1.12%. PM-DECT demonstrates similar performance on an anthropomorphic head phantom, retaining the appearance of fine and intricate sinus structures within decomposed images, while maintaining the ability to generate a CT image with comparable quality to that of a convention CT scan.

The design of primary modulation geometry and an iterative algorithm of signal processing is the key to the success of PM-DECT. Our unique iterative reconstruction algorithm with similarity based regularization produces decomposed images with a high level of spatial resolution and low noise. The retention of materials exhibiting very low contrast

can be a challenge as demonstrated by the acrylic rod in the contrast rod study. Despite this limitation, the contrast rod study shows that our method can accurately represent a variety of materials, including those with strong similarity to each other such as PMP, LDPE, and polystyrene. Also, it is noteworthy that as shown in Fig. 3.10 PM-DECT grants DECT capabilities without degrading CT image quality compared to a conventional scan. Thus, the generated decomposed images serve as additional information extracted from a single CT scan that would be otherwise unavailable.

CHAPTER 4

CONCLUSION AND FUTURE RESEARCH CONSIDERATIONS

In this dissertation we explored two methods addressing fundamental limitations of DECT that restrict its utility and application. In Chapter 2, we presented a unique method, known as IDEM, to suppress noise on DECT decomposed images and overcome the well known issue of noise amplification during material decomposition. By exploring the entropy property of measured signals within a 2D transformation space of decomposed image values, IDEM achieves noise suppression while circumventing the need to constrain spatial variations in signals. This grants IDEM the potential to preserve NPS and to break the tradeoff between noise suppression and the retention of spatial resolution.

Furthermore, the principle of entropy minimization may shed light on designs of data processing algorithms for advanced CT imaging that acquire spectral information of the scanned object, including multi-energy CT [54] and energy-resolved CT [55, 56]. In these future investigations, it will be important to remember that the IDEM method relies implicitly upon the assumption that the signals after basis material decomposition, if containing no noise, have a small number of different levels, which implies small entropy. In situations where this assumption becomes invalid, the IDEM method is expected to have limited efficacy. For example, for DECT decomposition in the projection domain, we expect the IDEM method to fail because projection images have signal values with a continuous distribution and thus large entropy.

In Chapter 3, we proposed a novel method, known as PM-DECT, to grant DECT capabilities during a single CT scan on a conventional scanner through limited hardware modification and thus potentially liberate DECT from specialized scanners, increasing its clinical availability. By utilizing a primary modulator to selectively harden an x-ray beam at specific detector locations, PM-DECT is able to achieve simultaneous collection of high

and low energy projection data during a single scan, from which PM-DECT's unique iterative algorithm with similarity based regularization jointly reconstructs CT and decomposed images with a high level of spatial resolution and low noise.

CBCT projection data and image quality are degraded by severe scatter contamination which alters pixel values and decreases contrast-to-noise ratios. Thus, scatter correction is essential for performing effective DECT on CBCT systems. The primary modulation technique was initially designed for scatter correction in CBCT, and now is an established method used by different research groups. Recent improvements permit greater flexibility in modulator design [48]. In future work, we will investigate the use of primary modulation for the enhancement of CBCT scans by combining DECT and scatter correction capabilities. One focus of our research will be to optimize PM-DECT so as to limit the potential effects of residual scatter, as well as other sources of error, during basis material decomposition.

Appendices

APPENDIX A

BEAM HARDENING

The average photon energy $\left(\overline{E}\right)$ of an x-ray beam is given as:

$$\overline{E} = \frac{\int_0^{E_{max}} E \cdot \Phi(E) \, \mathrm{d}E}{\int_0^{E_{max}} \Phi(E) \, \mathrm{d}E} \tag{A.1}$$

where $\Phi(E)$ is beam intensity as a function of photon energy. $\Phi(E)$ is determined by the following equation:

$$\Phi(E) = \Phi_0(E)e^{-\mu(E)L}. \tag{A.2}$$

where $\Phi_0(E)$ represents the initial intensity distribution prior to the beam's incidence upon an attenuating material, L is the length travelled through an attenuating material, and $\mu(E)$ defines the attenuation coefficient of a material as it varies with photon energy.

Due to the polyenergetic nature of diagnostic photon beams and the dependence of μ on photon energy, $\overline{E}$ changes as the beam passes through an attenuating medium. In the diagnostic energy range, μ increases as energy decreases. Consequently, an attenuating medium preferentially removes lower energy photons from the beam, and the average energy of the spectrum increases. This phenomenon is known as beam hardening. The realized shift in energy depends upon the initial photon spectrum as well as the material and thickness of the attenuating material. For example, simulation studies show that an x-ray spectrum generated at 125 kVp has an average energy of 54 keV. After passing through 0.406 mm of copper the average photon energy increases to 68 keV. If instead the beam passes through 0.381 mm of molybdenum, the average value is 78 keV.

REFERENCES

[1] T. R. Johnson, C. Fink, S. O. Schönberg, and M. F. Reiser, Eds., *Dual energy CT in clinical practice*. Springer Science & Business Media, 2011.

[2] T. R. Johnson, B. Krauss, M. Sedlmair, M. Grasruck, H. Bruder, D. Morhard, C. Fink, S. Weckbach, M. Lenhard, B. Schmidt, T. Flohr, M. F. Reiser, and C. R. Becker, "Material differentiation by dual energy CT: Initial experience," *European-radiology*, vol. 17, no. 6, pp. 1510–1517, 2007.

[3] K Deng, C Liu, R Ma, C Sun, X. M. Wang, Z. T. Ma, and X. L. Sun, "Clinical evaluation of dual-energy bone removal in CT angiography of the head and neck: Comparison with conventional bone-subtraction CT angiography," *Clinical Radiology*, vol. 64, no. 5, pp. 534–541, 2009.

[4] Y Li, G Shi, S Wang, S Wang, and R Wu, "Iodine quantification with dual-energy CT: Phantom study and preliminary experience with VX2 residual tumour in rabbits after radiofrequency ablation," *The British Journal of Radiology*, vol. 86, no. 1029, pp. 143–151, 2013.

[5] H. Chandarana, A. J. Megibow, B. A. Cohen, R. Srinivasan, D. Kim, C. Leidecker, and M. Macari, "Iodine quantification with dual-energy CT: Phantom study and preliminary experience with renal masses," *American Journal of Roentgenology*, vol. 196, no. 6, W693–W700, 2011.

[6] A. N. Primak, J. G. Fletcher, T. J. Vrtiska, O. P. Dzyubak, J. C. Lieske, M. E. Jackson, J. C. Williams, and C. H. McCollough, "Noninvasive differentiation of uric acid versus non–uric acid kidney stones using dual-energy CT," *Academic Radiology*, vol. 14, no. 12, pp. 1441–1447, 2007.

[7] A. Graser, T. R. Johnson, M. Bader, M. Staehler, N. Haseke, K. Nikolaou, M. F. Reiser, C. G. Stief, and C. R. Becker, "Dual energy CT characterization of urinary calculi: Initial in vitro and clinical experience," *Investigative radiology*, vol. 43, no. 2, pp. 112–119, 2008.

[8] M. Eiber, K. Holzapfel, M. Frimberger, M. Straub, H. Schneider, E. J. Rummeny, M. Dobritz, and A. Huber, "Targeted dual-energy single-source CT for characterisation of urinary calculi: Experimental and clinical experience," *European Radiology*, vol. 22, no. 1, pp. 251–258, 2012.

[9] L. Yu, J. A. Christner, S. Leng, J. Wang, J. G. Fletcher, and C. H. McCollough, "Virtual monochromatic imaging in dual-source dual-energy CT: Radiation dose and image quality," *Medical Physics*, vol. 38, no. 12, pp. 6371–6379, 2011.

[10] R. Yuan, W. P. Shuman, J. P. Earls, C. J. Hague, H. A. Mumtaz, A. Scott-Moncrieff, J. D. Ellis, J. R. Mayo, and J. A. Leipsic, "Reduced iodine load at CT pulmonary angiography with dual-energy monochromatic imaging: Comparison with standard CT pulmonary angiographya prospective randomized trial," *Radiology*, vol. 262, no. 1, pp. 290–297, 2012.

[11] N. Takahashi, R. P. Hartman, T. J. Vrtiska, A. Kawashima, A. N. Primak, O. P. Dzyubak, J. N. Mandrekar, J. G. Fletcher, and C. H. McCollough, "Dual-energy CT iodine-subtraction virtual unenhanced technique to detect urinary stones in an iodine-filled collecting system: A phantom study," *American Journal of Roentgenology*, vol. 190, no. 5, pp. 1169–1173, 2008.

[12] L.-J. Zhang, J. Peng, S.-Y. Wu, Z. J. Wang, X.-S. Wu, C.-S. Zhou, X.-M. Ji, and G.-M. Lu, "Liver virtual non-enhanced CT with dual-source, dual-energy CT: A preliminary study," *European Radiology*, vol. 20, no. 9, pp. 2257–2264, 2010.

[13] C. M. Sommer, C. B. Schwarzwaelder, W. Stiller, S. T. Schindera, U. Stampfl, N. Bellemann, M. Holzschuh, J. Schmidt, J. Weitz, L. Grenacher, *et al.*, "Iodine removal in intravenous dual-energy CT-cholangiography: Is virtual non-enhanced imaging effective to replace true non-enhanced imaging?" *European Journal of Radiology*, vol. 81, no. 4, pp. 692–699, 2012.

[14] B. Ruzsics, H. Lee, P. L. Zwerner, M. Gebregziabher, P. Costello, and U. J. Schoepf, "Dual-energy CT of the heart for diagnosing coronary artery stenosis and myocardial ischemia-initial experience," *European Radiology*, vol. 18, no. 11, pp. 2414–2424, 2008.

[15] G. Lu, Y Zhao, L. Zhang, and U. Schoepf, "Dual-energy CT of the lung," *American Journal of Roentgenology*, vol. 199, no. 11, S40–S53, 2012.

[16] L.-J. Zhang, S.-Y. Wu, J.-B. Niu, Z.-L. Zhang, H. Z. Wang, Y.-E. Zhao, X. Chai, C.-S. Zhou, and G.-M. Lu, "Dual-energy CT angiography in the evaluation of intracranial aneurysms: Image quality, radiation dose, and comparison with 3d rotational digital subtraction angiography," *American Journal of Roentgenology*, vol. 194, no. 1, pp. 23–30, 2010.

[17] A. A. Postma, P. A. Hofman, A. A. Stadler, R. J. van Oostenbrugge, M. P. Tijssen, and J. E. Wildberger, "Dual-energy CT of the brain and intracranial vessels," *American Journal of Roentgenology*, vol. 199, no. 5_supplement, S26–S33, 2012.

[18] R. E. Alvarez and A. Macovski, "Energy-selective reconstructions in x-ray computerised tomography," *Physics in Medicine and Biology*, vol. 21, no. 5, pp. 733–744, 1976.

[19] S. J. Riederer and C. Mistretta, "Selective iodine imaging using k-edge energies in computerized x-ray tomography," *Medical Physics*, vol. 4, no. 6, pp. 474–481, 1977.

[20] L. A. Lehmann, R. E. Alvarez, A. Macovski, W. R. Brody, N. J. Pelc, S. J. Riederer, and A. L. Hall, "Generalized image combinations in dual kvp digital radiography," *Medical Physics*, vol. 8, no. 5, pp. 659–667, 1981.

[21] E. Y. Sidky, Y. Zou, and X. Pan, "Impact of polychromatic x-ray sources on helical, cone-beam computed tomography and dual-energy methods," *Physics in Medicine and Biology*, vol. 49, no. 11, pp. 2293–2303, 2004.

[22] C. Maaß, M. Baer, and M. Kachelrieß, "Image-based dual energy CT using optimized precorrection functions: A practical new approach of material decomposition in image domain," *Medical Physics*, vol. 36, no. 8, pp. 3818–3829, 2009.

[23] P. Sukovic and N. H. Clinthorne, "Penalized weighted least-squares image reconstruction for dual energy x-ray transmission tomography," *IEEE Transactions on Medical Imaging*, vol. 19, no. 11, pp. 1075–1081, 2000.

[24] C. Maaß, E Meyer, and M. Kachelrieß, "Exact dual energy CT material decomposition from inconsistent rays (MDIR)," 2, vol. 38, American Association of Physicists in Medicine, 2011, pp. 691–700.

[25] X. Dong, T. Niu, and L. Zhu, "Combined iterative reconstruction and image-domain decomposition for dual energy CT using total-variation regularization," *Medical Physics*, vol. 41, no. 5, p. 051 909, 2014.

[26] T. Niu, X. Dong, M. Petrongolo, and L. Zhu, "Iterative image-domain decomposition for dual-energy CT," *Medical Physics*, vol. 41, no. 4, p. 041 901, 2014.

[27] W. A. Kalender, E. Klotz, and L. Kostaridou, "An algorithm for noise suppression in dual energy CT material density images," *IEEE Transactions on Medical Imaging*, vol. 7, no. 3, pp. 218–224, 1988.

[28] A Macovski, D. Nishimura, A Doost-Hoseini, and W. Brody, "Measurement-dependent filtering: A novel approach to improved SNR," *IEEE Transactions on Medical Imaging*, vol. 2, no. 3, pp. 122–127, 1983.

[29] R. J. Warp and J. T. Dobbins III, "Quantitative evaluation of noise reduction strategies in dual-energy imaging," *Medical Physics*, vol. 30, no. 2, pp. 190–198, 2003.

[30] M. Balda, B. Heismann, and J. Hornegger, "Value-based noise reduction for low-dose dual-energy computed tomography," in *International Conference on Medical Image Computing and Computer-Assisted Intervention*, Springer, 2010, pp. 547–554.

[31] T. Niu, X. Ye, Q. Fruhauf, M. Petrongolo, and L. Zhu, "Accelerated barrier optimization compressed sensing (ABOCS) for CT reconstruction with improved convergence," *Physics in Medicine and Biology*, vol. 59, no. 7, pp. 1801–1814, 2014.

[32] P. B. Noël, A. A. Fingerle, B. Renger, D. Münzel, E. J. Rummeny, and M. Dobritz, "Initial performance characterization of a clinical noise–suppressing reconstruction algorithm for MDCT," *American Journal of Roentgenology*, vol. 197, no. 6, pp. 1404–1409, 2011.

[33] K. L. Boedeker, V. N. Cooper, and M. F. McNitt-Gray, "Application of the noise power spectrum in modern diagnostic MDCT: Part i. measurement of noise power spectra and noise equivalent quanta," *Physics in Medicine and Biology*, vol. 52, no. 14, pp. 4027–4046, 2007.

[34] K. Boedeker and M. McNitt-Gray, "Application of the noise power spectrum in modern diagnostic MDCT: Part ii. noise power spectra and signal to noise," *Physics in Medicine and Biology*, vol. 52, no. 14, pp. 4047–4061, 2007.

[35] R. Rutherford, B. Pullan, and I Isherwood, "Measurement of effective atomic number and electron density using an EMI scanner," *Neuroradiology*, vol. 11, no. 1, pp. 15–21, 1976.

[36] A. Buades, B. Coll, and J.-M. Morel, "A review of image denoising algorithms, with a new one," *Multiscale Modeling & Simulation*, vol. 4, no. 2, pp. 490–530, 2005.

[37] T. Niu and L. Zhu, "Scatter correction for full-fan volumetric CT using a stationary beam blocker in a single full scan," *Medical Physics*, vol. 38, no. 11, pp. 6027–6038, 2011.

[38] P. T. Lauzier and G.-H. Chen, "Characterization of statistical prior image constrained compressed sensing. i. applications to time-resolved contrast-enhanced ct," *Medical Physics*, vol. 39, no. 10, pp. 5930–5948, 2012.

[39] J. Siewerdsen, I. Cunningham, and D. Jaffray, "A framework for noise-power spectrum analysis of multidimensional images," *Medical Physics*, vol. 29, no. 11, pp. 2655–2671, 2002.

[40] J Baek and N. Pelc, "The noise power spectrum in CT with direct fan beam reconstruction," *Medical Physics*, vol. 37, no. 5, pp. 2074–2081, 2010.

[41] G. D. Finlayson, M. S. Drew, and C. Lu, "Entropy minimization for shadow removal," *International Journal of Computer Vision*, vol. 85, no. 1, pp. 35–57, 2009.

[42] L. Zhu and J. StarLack, "A practical reconstruction algorithm for CT noise variance maps using FBP reconstruction," in *Medical Imaging*, International Society for Optics and Photonics, 2007, pp. 651 023–651 023.

[43] T. Niu and L. Zhu, "Accelerated barrier optimization compressed sensing (ABOCS) reconstruction for cone-beam CT: Phantom studies," 7, vol. 39, American Association of Physicists in Medicine, 2012, pp. 4588–4598.

[44] X. Dong, T. Niu, and L. Zhu, "Single-scan energy-selective imaging on cone-beam CT: A preliminary study," in *SPIE Medical Imaging*, International Society for Optics and Photonics, 2013, 86682Z–86682Z.

[45] L. Zhu, N. R. Bennett, and R. Fahrig, "Scatter correction method for x-ray CT using primary modulation: Theory and preliminary results," *IEEE Transactions on Medical Imaging*, vol. 25, no. 12, pp. 1573–1587, 2006.

[46] H Gao, R. Fahrig, N. R. Bennett, M Sun, J Star-Lack, and L. Zhu, "Scatter correction method for x-ray CT using primary modulation: Phantom studies," *Medical Physics*, vol. 37, no. 2, pp. 934–946, 2010.

[47] H. Gao, L. Zhu, and R. Fahrig, "Modulator design for x-ray scatter correction using primary modulation: Material selection," *Medical Physics*, vol. 37, no. 8, pp. 4029–4037, 2010.

[48] L. Zhu, "Local filtration based scatter correction for cone-beam CT using primary modulation," *Medical Physics*, vol. 43, no. 11, pp. 6199–6209, 2016.

[49] M. Petrongolo and L. Zhu, "Noise suppression for dual-energy CT through entropy minimization," *IEEE Transactions on Medical Imaging*, vol. 34, no. 11, pp. 2286–2297, 2015.

[50] T. Wang and L. Zhu, "Dual energy CT with one full scan and a second sparse-view scan using structure preserving iterative reconstruction (SPIR)," *Physics in Medicine and Biology*, vol. 61, no. 18, pp. 6684–6706, 2016.

[51] J. Harms, T. Wang, M. Petrongolo, T. Niu, and L. Zhu, "Noise suppression for dual-energy CT via penalized weighted least-square optimization with similarity-based regularization," *Medical Physics*, vol. 43, no. 5, pp. 2676–2686, 2016.

[52] M. Petrongolo, X. Dong, and L. Zhu, "A general framework of noise suppression in material decomposition for dual-energy CT," *Medical Physics*, vol. 42, no. 8, pp. 4848–4862, 2015.

[53] R. L. Siddon, "Fast calculation of the exact radiological path for a three-dimensional CT array," *Medical Physics*, vol. 12, no. 2, pp. 252–255, 1985.

[54] P Sukovle and N. Clinthorne, "Basis material decomposition using triple-energy x-ray computed tomography," in *Instrumentation and Measurement Technology Conference, 1999. IMTC/99. Proceedings of the 16th IEEE*, IEEE, vol. 3, 1999, pp. 1615–1618.

[55] R. E. Alvarez, "Dimensionality and noise in energy selective x-ray imaging," *Medical Physics*, vol. 40, no. 11, p. 111 909, 2013.

[56] K Taguchi and J. Iwanczyk, "Vision 20/20: Single photon counting x-ray detectors in medical imaging," *Medical Physics*, vol. 40, no. 10, p. 100 901, 2013.